



Configuration Interaction Approach to Atomic Nuclei: The Shell Model

Yusuke Tsunoda and Takaharu Otsuka

Contents

Introduction	3
Shell Structure and Magic Numbers: Traditional View	5
Shell-Model Calculation: CI Calculation Beyond the IPM	7
Valence Shell and Hamiltonian	8
Many-Body Schrödinger Equation	9
Single-Particle Energies for the Shell Model	12
Effective NN Interaction for the Shell Model	12
Example of Shell-Model Calculation	13
Monte Carlo Shell Model: Computational Breakthrough and More	15
Basic Formulation	15
Advanced Generation of Basis Vectors by Variational Method	18
Extrapolation to Exact Energy Eigenvalue	18
Additional Remarks on the MCSM	19
Shell Evolution Due to Monopole Interaction	20
Monopole Matrix Element and Monopole Interaction	21
Central, 2-Body Spin-Orbit and Tensor Parts of the NN Interaction	24
Monopole Interaction of the Central Force	25
Monopole Interaction of the Tensor Force	25
Monopole Interaction Effects from the Central and Tensor Forces Combined	26
$N=34$ New Magic Number as a Consequence of the Shell Evolution	28
Monopole Interaction of the 2-Body Spin-Orbit Force	29
Monopole Interaction from the Three-Nucleon Force	29
Short Summary of This Section	31

Y. Tsunoda (✉)

Center for Nuclear Study, University of Tokyo, Tokyo, Japan

Center for Computational Sciences, University of Tsukuba, Tsukuba, Ibaraki, Japan

e-mail: ytsunoda@nucl.ph.tsukuba.ac.jp

T. Otsuka (✉)

RIKEN Nishina Center, Wako, Hirosawa, Japan

Department of Physics, University of Tokyo, Tokyo, Japan

e-mail: otsuka@phys.s.u-tokyo.ac.jp

Correlations Among Valence Nucleons and Monte Carlo Shell Model	31
Shape Deformation, Quadrupole Interaction, and Rotational Band	31
Type II Shell Evolution	32
A Doubly Closed Nucleus ^{68}Ni	33
Deformed Shapes and Potential Energy Surface	34
Deformation Parameters and Comparison to Calculations with Gogny	
Interaction	38
T-Plot Analysis	39
Shell Evolution and Surface Deformation	43
Short Summary of This Section	46
Remarks	46
References	47

Abstract

The atomic nucleus comprises protons and neutrons, with complex quantum many-body structure, arising from these two kinds of constituents and also from complicated forces binding them (nuclear forces). Nevertheless, atomic nuclei exhibit simple and beautiful features, unexpected from the complexities. The gap between the complexity and the simplicity/beauty can be filled by the shell model, the nuclear physics terminology of configuration Interaction (CI) approach. This article presents basic ideas and formulations of the shell model, up to recent developments. The computational aspect is quite crucial for the shell model, because the Schrödinger equation has to be solved with the nuclear forces and the two kinds of fermions. The traditional approach based on direct diagonalization of Hamiltonian matrix has been used since the 1950s with technical improvements. Besides this approach, a different CI methodology, Monte Carlo shell model (MCSM), was proposed in the 1990s and has been developed. These methodologies are explained in a pedagogical way. Ni and Cu isotopes are discussed as examples of various appearances of low-lying deformed states coexisting with spherical ground states. The T-plot analysis is explained as a unique way to unveil nuclear shapes contained in the MCSM wave functions. The original version of the shell model was conceived by Mayer and Jensen. Recent studies show definite departures from this picture: the evolution of the shell structure, or the shell evolution, in exotic nuclei. The shell evolution is briefly sketched, with a certain emphasis on the prominent role of the tensor force. The shell evolution is extended from a single-particle-type feature to highly correlated many-body features such as the collective motion leading to surface deformation, as referred to as type II shell evolution. Thus, this article overviews the basic and contemporary facets of the nuclear shell model in simple terms.

Introduction

It is of particular interest to describe the quantum many-body structure of atomic nuclei, largely because the atomic nucleus is an isolated object comprising many protons and neutrons, called nucleons collectively, interacting through highly complex and yet strongly attractive forces, called nuclear forces. Visible materials in the universe, except for hydrogen atoms, are composed of atomic nuclei packed with nucleons bound by such nuclear forces. The description of atomic nuclei is a major challenge, however.

Such description was attempted with the picture of “compound nucleus” by Bohr (1936a), where the motion of nucleons is considered to be so chaotic that their individual motions cannot be traced in terms of single-particle degrees of freedom (see Fig. 1, Bohr 1936b, 1937). This picture looks like a quantum mechanical version of the liquid drop model in the classical-mechanical view.

With emerging experimental evidences pointing to single-particle features of atomic nuclei, about a decade later, Mayer (1949) and Jensen (Haxel et al. 1949) proposed the shell model, where protons and neutrons occupy single-particle orbits forming shells and magic numbers. As this description succeeded in explaining key experimental features, the shell model has become the standard theoretical framework and has been developed significantly in various directions. The initial view by Mayer and Jensen can be characterized as the independent particle model (IPM) with a proper potential. The aspects of many-body physics were developed, for instance, by Talmi (1962), treating the interactions between nucleons more explicitly. Over several decades, there have been significant developments (see, for instance, a review article (Caurier et al. 2005) or introductory textbooks Heyde 1994, 2004). The shell model has become an indispensable approach to describe and analyze the atomic nuclei based on the nucleon-nucleon (NN) interactions, without resorting to models and/or approximations linked directly to the features to

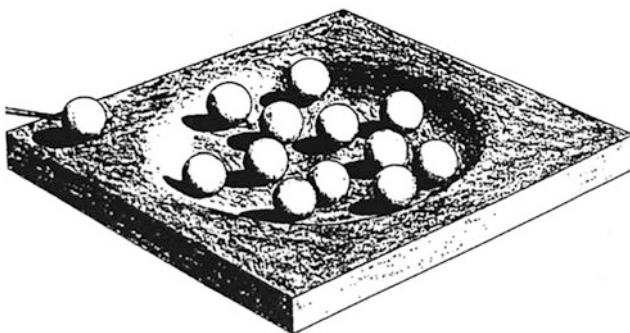


Fig. 1 Schematic illustration of the compound nucleus by Niels Bohr. (Taken from Fig. 1 of Bohr 1936b)

be described. In this short article, basic ideas and procedures of the shell model are presented. One of the advantages of the shell model is to include various correlations in many-body systems as the NN interactions produce. Representative features of them are sketched.

The atomic nucleus is composed of Z protons and N neutrons. Their sum is called the mass number $A = Z + N$. Among atomic nuclei, stable nuclei are characterized by their infinite or almost infinite lifetimes and are characterized by rather balanced Z to N ratios, with N/Z ranging from about 1 up to about 1.5. There are about 300 stable nuclei. Other nuclei are called exotic (or unstable) nuclei. The total number of exotic nuclei is unknown but seems to be between 7000 and 10,000, providing a huge show case of various properties as well as the paths of stellar nucleosynthesis (see, for instance, Gade and Glasmacher 2008; Nakamura et al. 2017; Sorlin and Porquet 2008). The exotic nuclei decay, through β (i.e., weak) processes, to other nuclei where Z and N are better balanced, as the β decay changes a neutron to a proton or vice versa. This decay occurs successively, until the process ends at a stable nucleus. Thus, only stable nuclei exist on earth, while exotic nuclei do not, being exotic literally. The shell model works equally well for stable and exotic nuclei, exhibiting both usual and unusual properties of these nuclei as consequences of nuclear forces. Features of exotic nuclei are a current frontier of nuclear physics, and this article is expected to provide a useful guide to ongoing and future studies on exotic nuclei.

After this Introduction in section “[Introduction](#)”, this article presents an overview of the traditional pictures of the shell structure and the magic number in section “[Shell Structure and Magic Numbers: Traditional View](#)”, along the IPM picture of Mayer and Jensen. The shell-model calculations including configuration mixings due to NN interactions are discussed in section “[Shell-Model Calculation: CI Calculation Beyond the IPM](#)”, beyond the IPM. The concepts like valence shell, model space, shell-model dimension, effective interaction, etc. will be introduced, but the methodology will be restricted to the traditional one by the matrix diagonalization. The Monte Carlo shell model (MCSM) will be introduced and explained in a rather pedagogical manner in section “[Monte Carlo Shell Model: Computational Breakthrough and More](#)”, as a breakthrough of major difficulty of the traditional method. Some of recent developments are presented there. The article then sheds light, in section “[Shell Evolution Due to Monopole Interaction](#)”, on a more conceptual development: the evolution of the shell structure with excess neutrons, abbreviated as *the shell evolution*, and its relation to the monopole interaction. The monopole effects from the central, tensor, and three-nucleon forces are sketched with some examples like the theoretical prediction and experimental verification of the new magic number $N = 34$. In section “[Correlations Among Valence Nucleons and Monte Carlo Shell Model](#)”, correlations among valence nucleons are discussed by referring to results of the MCSM calculations. Some basic concepts of nuclear ellipsoidal shapes will be presented, and MCSM wave functions are analyzed in terms of the T-plot. Type II shell evolution will be discussed for Ni isotopes, demonstrating the monopole and quadrupole interactions work together, yielding low-lying intruder deformed bands. The ground-state spin inversion in exotic Cu

isotopes, which is a typical shell evolution phenomenon, will be analyzed as to how it survives after the correlations by the NN interaction are included.

This article thus overviews basic formulation, current methodologies, and selected recent outcomes, as pedagogically as possible. The atomic nucleus might look like chaotic as N. Bohr conceived, once one looks into degrees of freedom involved. It is, fortunately, still possible to describe its structure starting from the interactions between its constituents, providing beautiful features with clean regularities. It is a great interest how far the shell model keeps penetrating into the incredible complexities of nuclear structure, identified as being chaotic by N. Bohr.

Shell Structure and Magic Numbers: Traditional View

Figure 2 depicts the basic idea and consequences of Mayer-Jensen's model. The nuclear matter composed of protons and neutrons is displayed in Fig. 2a: this matter shows an almost constant density of nucleons inside the surface which is a sphere as a natural assumption. Because of the short-range character of nuclear forces, this constant density results in a mean potential with a constant depth inside the surface, as shown in Fig. 2b. Let's assume that the density distribution is isotropic, producing an isotropic mean potential. Figure 2b also suggests that the harmonic oscillator (HO) potential is a good approximation to this mean potential as long as the mean potential shows negative values (or attraction) as a function of r , the radius from the center of the nucleus. The mean potential is then switched to the HO potential, which is analytically more tractable. Thus, the HO potential can be introduced from the constant density (sometimes referred to as "density saturation") and the short-range attraction due to nuclear forces.

The eigenstates of the HO potential are single-particle states shown in the far-left column of Fig. 2c with associated magic numbers and HO quanta, N . These HO magic numbers do not change by adding the minor correction of the ℓ^2 term, the scalar product of the orbital angular momentum \vec{l} (see the second column from left in Fig. 2c; for details see Bohr and Mottelson 1969).

The crucial factor introduced by Mayer and Jensen was the spin-orbit (SO) term, $(\vec{l} \cdot \vec{s})$, the effect of which is shown in the third column from left in Fig. 2c. The two orbits with the same orbital angular momentum, ℓ , and the same HO quanta are denoted as

$$j_{>} = \ell + 1/2 \text{ and } j_{<} = \ell - 1/2, \quad (1)$$

where $1/2$ is due to the spin, $s = 1/2$. The notation of $j_{>}$ and $j_{<}$ will be used throughout this article. The spin-orbit term,

$$v_{ls} = f_{ls}(\vec{l} \cdot \vec{s}), \quad (2)$$

is added to the $\text{HO} + \ell^2$ potential, where f_{ls} is the strength parameter. With $f_{ls} < 0$ as is the case for nuclear forces, the $j_{>}$ state is lowered in energy, whereas the

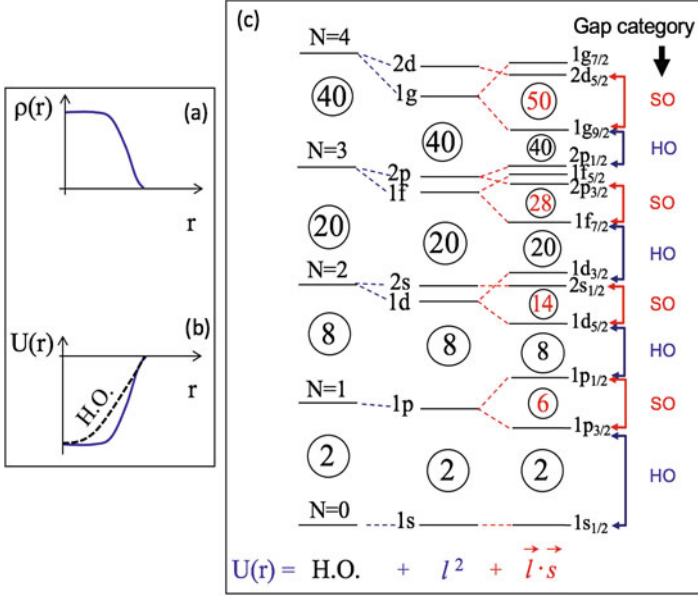


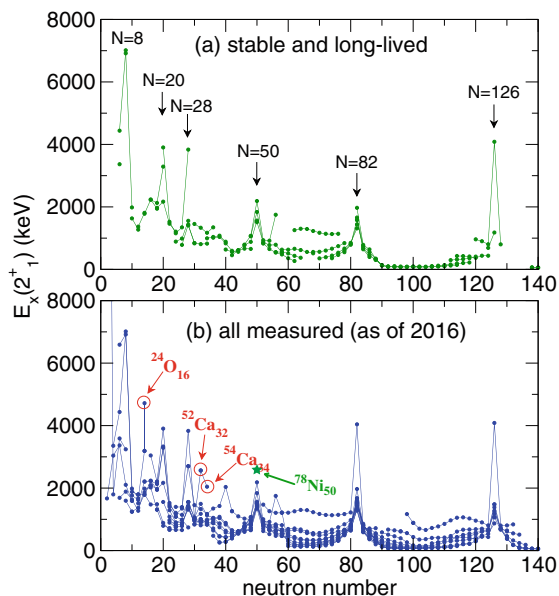
Fig. 2 Schematic illustration of (a) density distribution of nucleons in atomic nuclei, (b) a mean potential (solid line) produced by nucleons in atomic nuclei and an approximation by a harmonic oscillator (HO) potential (dashed line). In (a) and (b), the horizontal line denotes the radius from the center of the nucleus. (c) The shell structure produced and the resulting magic numbers in circles. (left column) Only the HO potential is taken with HO quanta shown as $N=0, N=1, \dots$ (N here does not mean the neutron number, N .) (middle column) The so-called ℓ^2 term is added to the HO potential, where the magic gaps are shown in circles. The single-particle orbits are labeled in the standard way to the left. (right column) The spin-orbit term, $(\vec{l} \cdot \vec{s})$, is included further, and magic gaps emerging from this term are shown in red. The single-particle orbits are labeled to the right, including $j = \vec{l} + \vec{s}$. The magic gaps are classified as “HO” and “SO” for the HO potential and the spin-orbit origins, respectively. (Taken from Fig. 2 of Otsuka et al. (2020), which was based on Ragnarsson and Nilsson 1995)

$j_{<}$ state is raised. The value of f_{1s} is known empirically to be about $-20A^{-2/3}$ MeV (see eq. (2-132) of Bohr and Mottelson 1969).

The final pattern of the single-particle energies (SPE) is shown schematically in Fig. 2c. The single-particle states are labelled in the standard way up to their j values, and both HO and spin-orbit magic gaps are indicated in black and red, respectively. The magic numbers have been considered to be $Z, N = 2, 8, 20, 28, 50, 82$, and 126 , because the effect of the spin-orbit term becomes stronger as j becomes larger. In fact, the magic numbers $28, 50, 82$, and 126 are all due to this effect. Instead, the HO magic numbers beyond 20 were considered to be absent or to show only minor effects. They shall be looked back on, from modern views of the nuclear structure covering stable and exotic nuclei.

It is now investigated to what extent magic gaps in Fig. 2c have been observed. Figure 3 displays the observed excitation energies of the first 2^+ states of even-

Fig. 3 Systematics of the first 2^+ excitation energies ($E_x(2^+)$), for (a) stable and long-lived nuclei and (b) all nuclei measured up to 2016, as functions of the neutron number. Peaks in (a) are labelled by the neutron number (N), while the names of the nuclei are displayed for some new points (red symbols and letters) in (b). In (b), the new data of ^{78}Ni (green symbol and letter) is added. (Modified from Fig. 4 of Otsuka et al. 2020)



even nuclei as a function of N , where even-even stands for even- Z -even- N . These excitation energies tend to be high at the magic numbers, because excitations across the relevant magic gap are needed. The conventional magic numbers of Mayer and Jensen, $N = 2, 8, 20, 28, \dots, 126$, are expected to arise, and sharp spikes are indeed seen at these magic numbers in Fig. 3a where the excitation energies are shown for stable and long-lived (i.e. meta stable) nuclei. The panel (b) includes all measured first 2^+ excitation energies as of 2016. In addition to the spikes in panel (a), one sees some new ones. One of them is at $N=40$, which corresponds to $^{68}\text{Ni}_{40}$, representing a HO magic gap at $N=40$. There are three others corresponding to the nuclei, $^{24}\text{O}_{16}$, $^{52}\text{Ca}_{32}$, and $^{54}\text{Ca}_{34}$, as marked in red in the panel. The 2^+ excitation energies of these nuclei are about a factor of two higher than the overall trend, suggesting that $N=16, 32$, and 34 can be magic numbers, although none of them is present in Fig. 2c.

These new possible magic numbers are consequences of what are missing in the argument for deriving magic gaps in Fig. 2c. This exciting subject will be discussed, but before that, the shell-model calculation will be formulated.

Shell-Model Calculation: CI Calculation Beyond the IPM

The shell model proposed by Mayer and Jensen is considered to be the independent-particle model (IPM), where nucleons stay forever in designated single-particle orbits of the given potential well. The actual nuclear structure cannot be so simple in general: nucleons scatter one another by the NN interaction and consequently may change their orbits. This kind of processes, being beyond the IPM, yields additional

piece of the binding energy, called correlation energies. One then has to evaluate and include the correlation energies into the theoretical description. In this section, a sketch how to perform such calculations is drawn from the general viewpoint, followed by two examples.

Valence Shell and Hamiltonian

The Hamiltonian is written in general as

$$\hat{H} = \hat{H}_0 + \hat{V}, \quad (3)$$

where \hat{H}_0 denotes the one-body term given by

$$\hat{H}_0 = \sum_j \epsilon_{0;j}^p \hat{n}_j^p + \sum_j \epsilon_{0;j}^n \hat{n}_j^n, \quad (4)$$

where $\hat{n}_j^{p,n}$ means the proton or neutron number operator for the orbit j and $\epsilon_{0;j}^{p,n}$ implies proton or neutron SPE of the orbit j . This SPE is composed of the kinetic energy of the orbit j and the energy shift of the orbit j produced by all nucleons in the inert core.

In Eq.(3), \hat{V} stands for the nucleon-nucleon (NN) interaction, written in the standard way as

$$\hat{V} = \frac{1}{4} \sum_{\alpha,\beta,\gamma,\delta} v_{\alpha\beta\gamma\delta} a_{\alpha}^{\dagger} a_{\beta}^{\dagger} a_{\delta} a_{\gamma}, \quad (5)$$

where α, β, γ , and δ are single-particle states of nucleons. The labels α, β, γ , and δ denote the orbital j , its magnetic substate m , and the index of proton or neutron of each state. Here, $v_{\alpha\beta\gamma\delta}$ denotes an antisymmetric two-body matrix element of the interaction \hat{V} .

The single-particle states appearing in Eqs. (4), (5) are explained now. Single-particle orbits are assumed as shown in Fig. 2. Note that each single-particle state is a magnetic substate of one of the single-particle orbit j . The single-particle orbits of a given nucleus are generally grouped into closed shell, valence shell, and higher shells as shown in Fig. 4a. The closed shell comprises the orbits lowest in energy and are fully occupied (see the blue boxes in Fig. 4). The valence shell is partly occupied as indicated by green boxes in Fig. 4. Protons (neutrons) in the valence shell are called valence protons (neutrons), which are frequently mentioned in shell-model studies. Likewise, single-particle orbits in the valence shell are referred to as valence orbits and so on. In shell-model calculations, the single-particle orbits above the valence shell are treated to be empty.

The effective NN interaction is defined for valence nucleons, while effects of virtual excitations of nucleons to higher orbits are supposed to be implicitly included

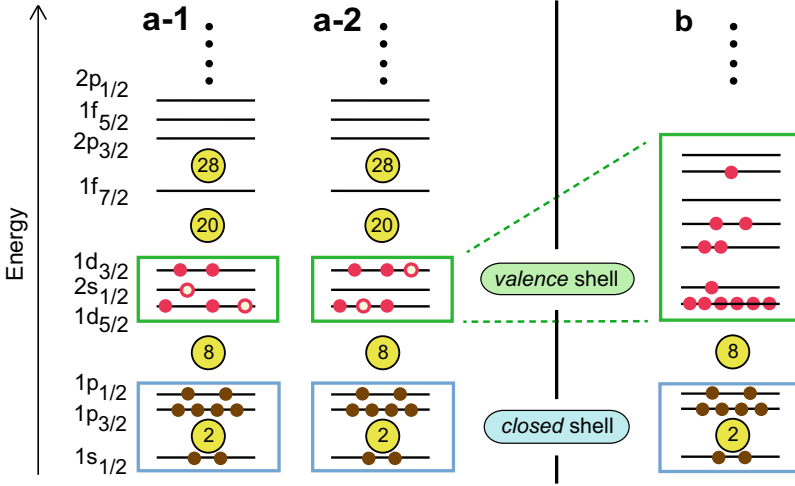


Fig. 4 Schematic illustrations of the shells and the magic numbers of neutrons. (The same feature appears for protons.) Horizontal bars indicate the energies of single-particle orbits, labelled to the left. Magic numbers are shown in larger circles with yellow highlight. Filled and open small circles imply neutrons. The lowest three orbits ($1s_{1/2}$, $1p_{3/2,1/2}$) are fully occupied, forming the *closed shell* (blue box). On top of it, the next shell between the magic numbers 8 and 20, called the *sd shell*, is partially occupied. If a shell is partially occupied, it is called a *valence shell* (green box). (a-1, a-2) Different occupation patterns in the *sd shell* as the valence shell. Two neutrons shown by open circles in panel (a-1) scatter each other, and resulting in panel (a-2), causing a configuration mixing. Shells above the magic number 20 are empty. The shell consisting of the $2p_{1/2,3/2}$, $1f_{5/2,7/2}$ is called the *pf shell*. (b) Two major shells, *sd* and *pf*, are merged, and neutrons are distributed over the *sd-pf shell*

in this effective NN interactions through their renormalization. In general, there are certain variations of the effective NN interaction for a given valence shell, corresponding to its origin, derivation, tunings, *etc.* Common features and varying properties of such effective NN interactions shall be discussed.

Figure 4a and b depicts different valence shells: panels a-1 and a-2 represent normal shell structure à la Mayer and Jensen, while panel b schematically displays shell structure that may appear, for instance, in some exotic nuclei, as two conventional shells are merged into a new single shell.

Thus, \hat{V} in Eq. (3) actually refers to effective NN interactions between valence (i.e. active) nucleons. This means that the single-particle states in Eq. (5) are among those of the valence shell.

Many-Body Schrödinger Equation

The purpose of the shell-model calculation is to solve the many-body Schrödinger equation,

$$\hat{H}\Psi = E\Psi, \quad (6)$$

where Ψ is an eigenstate for an eigenvalue E . This general problem is solved within the valence shell by expanding Ψ in terms of many-body states in the valence shell for the given numbers of valence protons and valence neutrons. To be ideal, such many-body states are given by a complete set of the many-body states with these valence particles. A natural choice is given by all possible Slater determinants formed by valence protons and neutrons in the valence shell. Such Slater determinants are represented as

$$\phi_1, \phi_2, \dots, \phi_i, \dots, \text{ and } \phi_{n_d}, \quad (7)$$

where n_d is the total number of all possible Slater determinants, and

$$\phi_i = a_{\alpha_i}^\dagger a_{\beta_i}^\dagger \dots |0\rangle, \quad (8)$$

with $|0\rangle$ being the appropriate closed shell (see blue boxes in Fig. 4).

The matrix elements,

$$\langle \phi_1 | H | \phi_1 \rangle, \langle \phi_1 | H | \phi_2 \rangle, \dots, \langle \phi_{n_d} | H | \phi_{n_d} \rangle, \quad (9)$$

form the Hamiltonian matrix

$$H = \begin{pmatrix} \langle \phi_1 | H | \phi_1 \rangle & \langle \phi_1 | H | \phi_2 \rangle & \dots & \langle \phi_1 | H | \phi_{n_d} \rangle \\ \langle \phi_2 | H | \phi_1 \rangle & \langle \phi_2 | H | \phi_2 \rangle & \dots & \langle \phi_2 | H | \phi_{n_d} \rangle \\ \dots & \dots & \dots & \dots \\ \langle \phi_{n_d} | H | \phi_1 \rangle & \langle \phi_{n_d} | H | \phi_2 \rangle & \dots & \langle \phi_{n_d} | H | \phi_{n_d} \rangle \end{pmatrix}. \quad (10)$$

With this matrix, the Schrödinger equation is rewritten as

$$\begin{pmatrix} \langle \phi_1 | H | \phi_1 \rangle & \langle \phi_1 | H | \phi_2 \rangle & \dots & \langle \phi_1 | H | \phi_{n_d} \rangle \\ \langle \phi_2 | H | \phi_1 \rangle & \langle \phi_2 | H | \phi_2 \rangle & \dots & \langle \phi_2 | H | \phi_{n_d} \rangle \\ \dots & \dots & \dots & \dots \\ \langle \phi_{n_d} | H | \phi_1 \rangle & \langle \phi_{n_d} | H | \phi_2 \rangle & \dots & \langle \phi_{n_d} | H | \phi_{n_d} \rangle \end{pmatrix} \begin{pmatrix} c_1 \\ c_2 \\ \dots \\ c_{n_d} \end{pmatrix} = E \begin{pmatrix} c_1 \\ c_2 \\ \dots \\ c_{n_d} \end{pmatrix}. \quad (11)$$

where c_i 's are amplitudes, and the corresponding eigenstate Ψ is given by the superposition

$$\Psi = \sum_i c_i \phi_i. \quad (12)$$

In most of practical calculations, the a_μ^\dagger creates a proton or neutron (specified by μ) in the state μ which is the magnetic substate with a definite z-component j_z of the angular momentum j . In this scheme, the total value of j_z s, denoted as J_z , is a

definite value. The Hamiltonian H conserves the total angular momentum, J , and its z-component, and its eigenvalue does not change among states differing only in J_z . This means that if the Schrödinger equation is solved for one of $J_z = -J, -J+1, \dots, J-1, J$, one obtains all the essential information. Thus, the above calculation is carried out for one of the J_z values, and the Slater determinants in Eq. (8) are taken from those having the specified J_z value. The n_d value is then called *shell-model dimension*, which equals the dimension of the matrix in Eq. (10). For a fixed J , $J_z = \pm J$ is taken usually, because the shell-model dimension is smaller than the cases of $|J_z| < J$. It is noted that because of the time-reversal invariance, the n_d value does not change if only J_z changes its sign but all the other quantum numbers remain unchanged. Obviously, the shell-model dimension, n_d , indicates the size or the difficulty of the calculation from the viewpoint of the numerical computation. If there is only one valence orbit and only one valence nucleon, the shell-model dimension is one. But this dimension increases very rapidly as the number of valence orbits increases or the number of valence nucleons increases. Figure 5 exhibits the increase of the shell-model dimension as a function of the year of the publication or the actual calculation. It is noted that the dimension for the ^{32}Mg case is much larger than other nuclei with $A \sim 30$, because two shells, sd and pf , are merged in this case as shown in Fig. 4b (see Tsunoda et al. 2020).

There are quite a few computer codes for performing shell-model calculations. Among those being used widely, ANTOINE (Caurier and Nowacki 1999), BIGSTICK (Johnson et al. 2013), KSHELL (Shimizu et al. 2019), and NuShellX (Brown and Rae 2014) are accessible. These shell-model calculations are based on

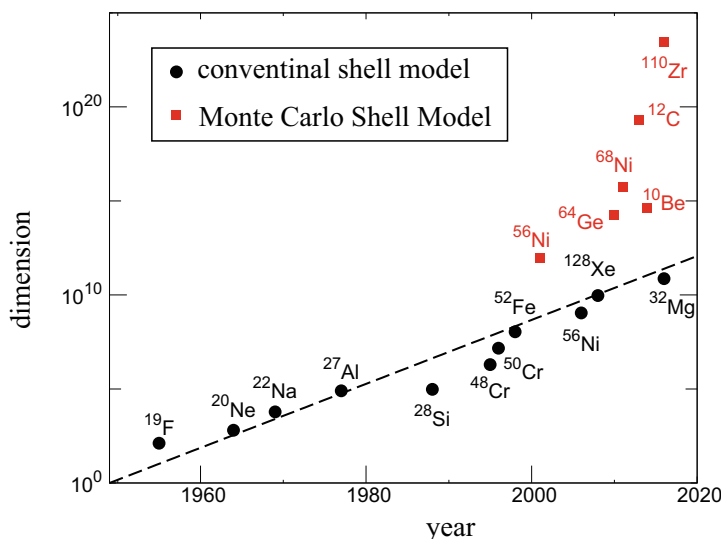


Fig. 5 Shell-model dimension as a function of the year. The maximum value of the shell-model dimension is indicated with the name of the nucleus for the year of the paper publication or the actual calculation. (Modified from Fig. 6 of Shimizu et al. 2017)

the traditional scheme besides many sophisticated technicalities. In addition to such traditional shell-model calculations, the Monte Carlo shell model has been proposed in order to overcome the difficulty of the shell-model dimension stated above.

Single-Particle Energies for the Shell Model

The single-particle energies (SPE) in Eq. (4) are one of the essential factors of the shell-model calculations. These values are either empirically obtained from measured values or calculated from fundamental principles. In this article, because of the length limitation, how to fix these values is not discussed, and in the examples discussed below, the SPEs are estimated, in some proper ways, with respect to the relevant closed shells. The most naïve way is to take their values from the experimental energy levels of the nuclei comprising a closed shell plus a nucleon. In many cases, the values of the SPEs are fitted so as to reproduce a large number of observed energy levels. This latter method has been shown to work quite well.

Effective NN Interaction for the Shell Model

The interaction \hat{V} in Eq. (3) (or Eq. (5)) is another crucial input to the shell-model calculation. It is often called the shell-model interaction. It is expressed in terms of the so-called two-body-matrix element (TBME) defined as

$$\langle j_1, j_2 ; J, T | \hat{V} | j_3, j_4 ; J, T \rangle, \quad (13)$$

where j_1, \dots stand for the valence orbits and J and T imply, respectively, the angular momentum and the isospin formed by the two-nucleon system being considered. As discussed above, \hat{V} conserves the J value, and the same J should appear in the ket and bra states. Usually the isospin is conserved by the NN interaction, keeping T as well. The rotational invariance of \hat{V} makes the TBME independent of J_z if all the other quantum numbers are unchanged. Thus the TBME in Eq. (13) is independent of J_z .

The TBMEs have been obtained for various valence shells. When the effective interaction \hat{V} is discussed, the valence shell is often called the *model space*, which may be done also in this article. Because of various renormalization effects coming from single-particle orbits below and/or above the valence shell, \hat{V} varies, in principle, as the model space is changed.

In early studies, the TBMEs were fitted purely empirically, for instance, for nuclei with $3 \leq Z \leq 8$ (Cohen and Kurath 1965). This kind of approach was limited up to $Z=10$ (Ne) (Arima et al. 1968). After a number of valuable attempts to obtain effective interactions, the so-called realistic shell-model interaction was obtained for the *sd*-shell nuclei ($8 \leq Z, N \leq 20$), named USD (-family) (Brown and Wildenthal 1988), with further extensions, USDA and USDB (Brown and Richter 2006; Richter et al. 2008). The effective interaction for the *pf*-shell nuclei

($20 \leq Z, N \leq 40$) was obtained as the KB3 (-family) interaction (Poves and Zuker 1981) and later as the GXPf1 (-family) interaction (Honma et al. 2002, 2004). These interactions were obtained in two steps: the starting point was given by microscopic G-matrix NN interactions proposed initially by Kuo and Brown (Hjorth-Jensen et al. 1995; Kuo and Brown 1966), and as the second step, certain phenomenological improvements were made by the fit to large numbers of experimental energy levels. It is mentioned that some main features, for instance, the tensor force component, remain unchanged by this fit (Otsuka et al. 2010a). Many other valuable shell-model interactions, for instance, (so-called) Kuo-Herling (Brown 2000), $sn100pn$ (Brown et al. 2005), JUN45 (Honma et al. 2009), and LNPS (Lenzi et al. 2010) interactions, have been constructed from the G-matrix interactions sometimes with refinements like monopole adjustments. It should be noticed that these shell-model interactions are derived microscopically to a large extent and that they should be distinguished from purely phenomenological interactions in earlier times mentioned above. The M3Y interaction (Bertsch et al. 1977) is related to the G-matrix, too. The original methodological and conceptual contribution of the so-called G-matrix approach to the effective NN interaction (Hjorth-Jensen et al. 1995; Kuo and Brown 1966) is highly appreciated.

The effective NN interaction was derived, more recently, from the chiral effective field theory (EFT) interaction, e.g. Machleidt and Entem (2011). It is first processed by the V_{low-k} method (Bogner et al. 2002; Nogga et al. 2004), the similarity renormalization group (SRG) method (Bogner et al. 2010), or by other methods for transforming the nuclear forces in the free space into tractable forms for further treatments. The outcome is then processed by the in-medium SRG method (Hergart et al. 2016), by the extended Krenciglowa-Kuo (EKK) method (Takayanagi 2011a,b; Tsunoda et al. 2014a), or other methods for incorporating medium effects like the core polarization. The V_{low-k} method has been adopted for the derivation of some modern shell-model interactions, for instance, the one by Coraggio *et al.*, for Sn (Coraggio et al. 2009) and Cr-Fe (Amswald et al. 2017) regions as well as the EEdf1 interaction (Tsunoda et al. 2017). The EEdf1 interaction has been applied to various studies for the nuclei around $N=20$ up to the neutron dripline (see Tsunoda et al. 2020). The SRG and IM-SRG methods have been studied extensively also but are not discussed in this article due to the length limitation.

Example of Shell-Model Calculation

The result of the calculation with the GXPf1 interaction for ^{57}Ni is shown in Fig. 6 as an example of the shell-model calculation (Honma et al. 2004). One sees a remarkable agreement between the calculation and the experiment. The GXPf1 interaction was not fitted particularly to the nucleus ^{57}Ni . There have been a large number of shell-model calculations, as good fractions of them are reviewed in Caurier et al. (2005) and Otsuka et al. (2020). It should be stressed that such shell-model calculations have significantly contributed to deeper and wider understanding

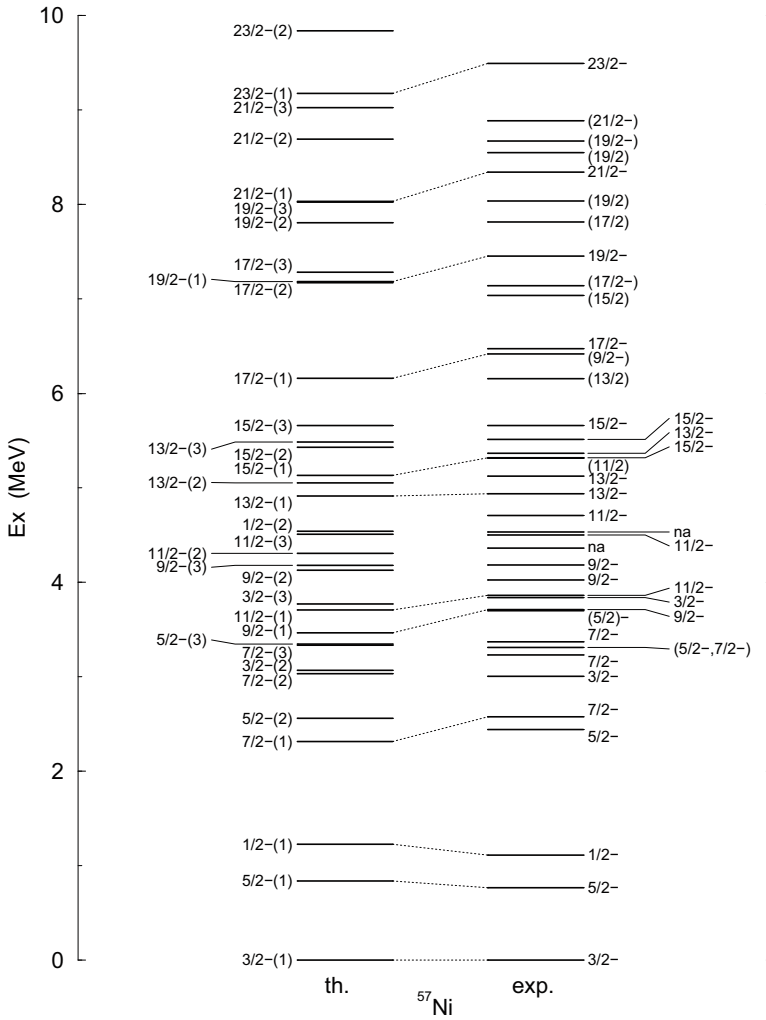


Fig. 6 Energy levels of ^{57}Ni as a typical example of the shell model calculation. The results obtained from the GXPFI1A interaction (th.) are compared to the experimental ones (exp.). Yrast levels (energetically lowest states for a given spin/parity) are connected by dotted lines. (Taken from Fig. 19 of Honma et al. 2004)

of the quantum many-body structure contained in experimental data on stable and exotic nuclei.

The diversity in the shell-model applications to interdisciplinary researches may be exemplified with the nuclear matrix element (NME) of the neutrinoless double beta decay. This quantity has been calculated in a variety of theoretical approaches, as shown in Fig. 7. The NME is needed to derive the neutrino mass from the lifetime of this decay, among other factors needed as well, see, for instance, a recent review

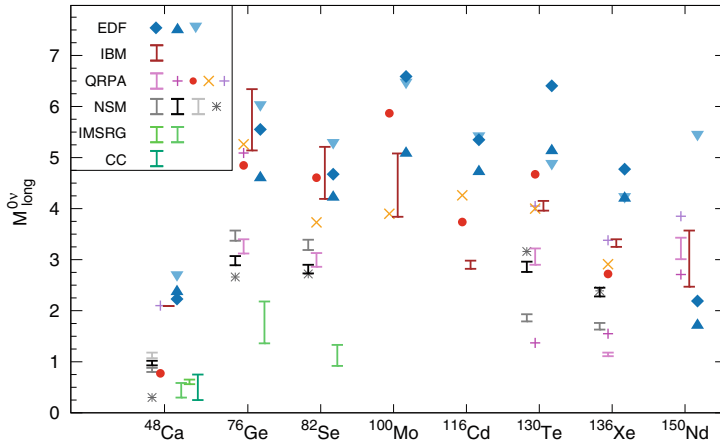


Fig. 7 Nuclear matrix elements of neutrinoless double beta decay calculated by various theoretical methods. The mother nuclei are shown below the panel. The shell model results are shown as “NSM” in the inset. (Taken from Fig. 8 of Agostini et al. 2022)

(Agostini et al. 2022). Figure 7 suggests rather smaller values by the shell model than other theoretical calculations. As various correlations contribute to the NME, the shell model should play crucial roles because different correlations are treated on an equal footing.

Monte Carlo Shell Model: Computational Breakthrough and More

The shell-model calculation is a powerful method to describe nuclear properties starting from a given NN interaction. It does not depend on a particular model assumption for the result to be obtained. However, the actual application encounters a difficulty of the huge shell-model dimension. Figure 5 shows the dimensions for various nuclei with relevant model spaces. Certainly, there are interesting and important cases beyond the limit.

Basic Formulation

The Monte Carlo shell model (MCSM) has been proposed and developed in order to overcome this dimension problem (Honma et al. 1995; Otsuka et al. 1998, 2001a; Shimizu et al. 2012, 2017). As the shell-model dimension is the major obstacle for the conventional shell-model calculation, the MCSM can be regarded as a game changer, because many cases with much larger shell-model dimensions become tractable. In this section, the outline of the MCSM is presented.

The k -th eigenstate of spin/parity J^π is expressed in the MCSM as

$$\Psi(J^\pi, k) = \sum_i f_i(J^\pi, k) \hat{P}(J^\pi) \Phi_i(J^\pi), \quad (14)$$

where i is the index of the basis vector and $\Phi_i(J^\pi)$ and $f_i(J^\pi, k)$ mean, respectively, the i -th basis vector, which is a Slater determinant, and its amplitude. It is noted that the basis vectors, $\Phi_i(J^\pi)$, $i = 1, 2, \dots$, are selected for the specific J^π . This amplitude is scaled so that the state $\Psi(J^\pi, k)$ is normalized. It is stressed here that the sets $\{\Phi_i; i = 1, 2, \dots\}$ and $\{f_i; i = 1, 2, \dots\}$ vary as functions of J^π . The z -component J_z is not shown here, because the energy eigenvalue remains unchanged if only J_z is varied. In actual calculations, one of possible J_z values is taken. The J_z dependences of other physical observables are known and are correctly treated in actual applications. In some case, an additional quantum number(s), such as the isospin, may have to be specified, but the required extension is trivial and is not discussed here. The symbol $\hat{P}(J^\pi)$ implies the projection onto the quantum number J^π , and it must project on the J_z chosen as stated above, but this process is not explicitly argued here for brevity. The J^π projection contains some technical complexities as stated elsewhere.

Equation (14) resembles Eq. (12), but there are distinct differences. One of clear differences lies in the basis vectors: the basis vector ϕ_i in Eq. (12) is a Slater determinant given by the product of usual single-particle states as shown in Eq. (8). On the other hand, the basis vector Φ_i in Eq. (14) is a Slater determinant given by the product,

$$\Phi_i(J^\pi) = b_1^{\dagger(J^\pi, i)} b_2^{\dagger(J^\pi, i)} \dots |0\rangle, \quad (15)$$

where the proton or neutron creation operator b^\dagger is defined as

$$b_m^{\dagger(J^\pi, i)} = \sum_n D_{n,m}^{(J^\pi, i)} a_n^\dagger, \quad m = 1, 2, \dots. \quad (16)$$

Here D denotes a matrix element, and a^\dagger already appeared in Eq. (8). Equation (16) implies that the operator b^\dagger is a proton or neutron creation operator for a state given by a superposition of all single-particle states in the model space. This superposition can make each Φ_i more optimum in the description of the eigenstates of the specified J^π value. It is noted that each MCSM basis vector can be called a “deformed” Slater determinant where single-particle states are superpositions of the original single-particle states (e.g., those of the HO potential). In this point, Eq. (14) differs from Eq. (12). Another major difference is the projection operator $\hat{P}(J^\pi)$.

The matrix \mathbf{D} thus transforms the original (naïve) single-particle states to the single-particle states specific for the i -th MCSM basis vector for the specific eigenstate of the designated J^π value. Thus, it has a superscript labelling (J^π, i) (see Eq. (16)). The search for the optimum D is crucial for the actual MCSM calculations.

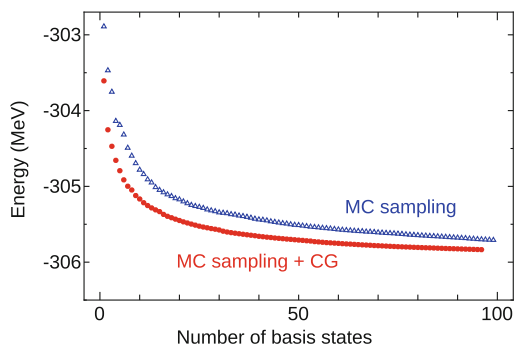
The matrix \mathbf{D} is fixed successively. One can start with an initial guess, denoted by u , of the first MCSM basis vector $\Phi_{i=1}(J^\pi)$, utilizing mean-field techniques, e.g., a deformed Hartree-Fock (HF) calculation for the shell-model Hamiltonian being used. Another candidate, denoted by v , is generated by a random minor change of u , and the energy is calculated from v . If this energy of v is lower than the energy of u , u is abandoned, and v is kept for the next step. If the other way around, v is rejected, and u is carried over to the next step. This competition process is repeated until the energy gain is saturated, meaning that the gain cannot exceed the prefixed minimum requirement, after some trials. The first MCSM basis vector, $\Phi_{i=1}(J^\pi)$, is thus determined. In short, it is a search for an optimum “deformed” Slater determinant by utilizing random variations of candidate states. As the deformed HF is obtained without the angular momentum projection but the present MCSM process is performed with good angular momentum and parity, the obtained $\Phi_{i=1}(J^\pi)$ naturally differs from the deformed HF state.

Figure 8 shows an example for the 0_1^+ ground state of ^{64}Ge nucleus (Shimizu 2013). The energy monitored is the ground-state energy in this case. The blue symbols (labelled “MC sampling”) indicate an MCSM calculation, and $\Phi_{i=1}(J^\pi)$ gives the energy slightly above -303 MeV. The second basis $\Phi_{i=2}(J^\pi)$ is searched similarly. It is different from the $i=1$ process in that the energy is calculated in a two-dimensional space spanned by the current trial state and the first basis vector $\Phi_{i=1}(J^\pi)$ which has been fixed. The number of basis vectors, denoted by n_b , is two now, and the eigenvalue of $n_b=2$ is indicated around -303.5 MeV by the blue symbol in Fig. 8.

Once the second basis vector $\Phi_{i=2}(J^\pi)$ is fixed, the third basis vector is searched in a similar way. With this successive process, $\Phi_{i=1}(J^\pi)$, $\Phi_{i=2}(J^\pi)$, $\Phi_{i=3}(J^\pi)$, ..., $\Phi_{i=n_b}(J^\pi)$ are obtained. These basis vectors are collectively called MCSM basis vectors and are actually represented by the matrix $\mathbf{D}^{(J^\pi, i)}$, $i = 1, 2, 3, \dots, n_b$.

It is mentioned that the MCSM basis vectors, $\Phi_i(J^\pi)$, $i = 1, 2, \dots$, are not mutually orthogonal. They are, however, linearly independent, and this independence gives additional dimensions to the many-body Hilbert space of the MCSM calculation. It is noted that because each basis vector takes the form of Slater determinant, the non-orthogonality is inevitable.

Fig. 8 Convergence pattern of the ground-state energy from an example case with ^{64}Ge . (Modified from Fig. 3 of Shimizu 2013)



By adding basis vectors, the energy eigenvalue is lowered. In other words, the calculated energy eigenvalue decreases as a function of n_b . The blue symbol in Fig. 8 displays such energy eigenvalues for each value of n_b . The eigenvalue comes down to about -305.7 MeV at $n_b=100$, where the eigenvalue is changing rather slowly, providing an expectation that the exact value may not be too far. Nevertheless, it is desired to have a quicker convergence to the exact eigenvalue.

Advanced Generation of Basis Vectors by Variational Method

The basis vector generation process has substantially been improved by introducing a variational process. A basis vector $\Phi_i(J^\pi)$ is good in the level of random search, but in general, there is a certain room of the improvement because the random search is a discrete sampling and may miss possible improvements between sampled cases. Once the basis vector $\Phi_i(J^\pi)$ is fixed by the random sampling, it is improved by the variational process called the conjugate gradient (CG) method (Shimizu 2013). In this process, the variation is made on the matrix $\mathbf{D}^{(J^\pi, i)}$ following the prescription of the CG method, monitoring the energy calculated with the angular momentum and parity projections. Thus an advanced version of the MCSM has been achieved.

Red symbols in Fig. 8 display the energy eigenvalues obtained by this advanced version. Figure 8 implies that this process produces a considerable effect, more than 0.7 MeV, already for the first basis vector ($n_b=1$). The convergence is improved also, and the derivative becomes smaller near $n_b=100$.

Extrapolation to Exact Energy Eigenvalue

Figure 8 depicts that the energy eigenvalues are on trajectories converging to the exact value. The plot in Fig. 8 may not be the best way for estimating the exact eigenvalue, as n_b can be as large as 10^{14} in this case. Of course, the convergence occurs much earlier, but it is computationally heavy to trace the evolution of the eigenvalue as a function of n_b .

Instead, a very powerful method has been introduced, as briefly explained below. The temporary energy eigenvalue corresponding to the number of the adopted basis vectors, n_b , is denoted by $E^{(J^\pi, k)}(n_b)$, and its eigen wavefunction is by $\Omega^{(J^\pi, k)}(n_b)$. In other words, $\Omega^{(J^\pi, k)}(n_b)$ is the eigen wave function, when the Schrödinger equation is solved with these n_b basis vectors. Thus, $\Omega^{(J^\pi, k)}(n_b)$ generally differs from the exact eigen wave function, while the former may serve as a good approximation to the latter. It is now attempted to gauge the difference between the two. First, the following quantity is introduced,

$$E^{(J^\pi, k)}(n_b) = \langle \Omega^{(J^\pi, k)}(n_b) | \hat{H} | \Omega^{(J^\pi, k)}(n_b) \rangle \quad (17)$$

where \hat{H} is the Hamiltonian defined in Eq. (3). The energy variance is then defined as

$$\Delta^{(J^\pi, k)}(n_b) = \langle \Omega^{(J^\pi, k)}(n_b) | \hat{H}^2 | \Omega^{(J^\pi, k)}(n_b) \rangle - \langle \Omega^{(J^\pi, k)}(n_b) | \hat{H} | \Omega^{(J^\pi, k)}(n_b) \rangle^2. \quad (18)$$

Both terms on the right-hand side are real numbers due to the hermiticity of \hat{H} . The variance $\Delta^{(J^\pi, k)}(n_b)$ is positive definite or zero. It is pointed out that $\Delta^{(J^\pi, k)}(n_b)$ becomes vanished if $\Omega^{(J^\pi, k)}(n_b)$ happens to be an eigenstate of \hat{H} . Figure 9 shows $E^{(J^\pi, k)}(n_b)$ against $\Delta^{(J^\pi, k)}(n_b)$ for $J^\pi = 0_1^+$ (ground state) and $J^\pi = 2_1^+$, where the index k is shown as the superscripts. (The index k will be indicated in this way hereafter.) Namely, each symbol is plotted at the coordinate designated by the variance, $\Delta^{(J^\pi, k)}(n_b)$, on the horizontal axis and the expectation value, $E^{(J^\pi, k)}(n_b)$, on the vertical axis. Thus, the left edge of the panel stands for the variance equal to zero, implying the exact solution. For the 0_1^+ state, the calculations with the variational improvement (red symbol) and without it (blue symbol) are shown. It is clear that the plots can be extrapolated by smooth curves. The plotted energies are fitted by

$$E = E_0 + a \Delta^{(J^\pi, k)}(n_b) + b \{\Delta^{(J^\pi, k)}(n_b)\}^2 + \dots \quad (19)$$

where E is the energy and E_0 is the value of E with a vanished variance. As mentioned above, E_0 is the exact eigenvalue, if the fit works as expected. The energy fitted with the polynomial up to the quadratic term is shown by lines in Fig. 9. One sees that the fit indeed works well.

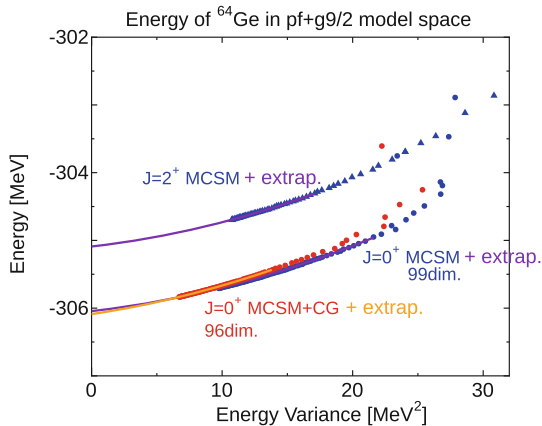
Thus, quite reliable values for the energies can be obtained. It is further emphasized that the excitation energies converge earlier than the energies themselves, as demonstrated by Fig. 9.

Additional Remarks on the MCSM

In many actual MCSM calculations, the energies of several eigenstates of a given J^π are monitored, for instance, by their average, in the generation process of the MCSM basis vectors. That kind of calculations are more sophisticated than those monitoring the energy of a single eigenstate but can be done. By doing this, the results for those states are obtained at once, and the orthogonalities among the obtained eigenstates are guaranteed. It is noted, however, that the accuracy may somewhat vary among those states.

It is mentioned that the quasi-particle vacua shell model (QVSM), which is the most advanced extension of the MCSM, has recently been proposed, where the basis vectors are not Slater determinants but particle-number-projected quasi-particle vacua (Shimizu et al. 2021). Like the Bogoliubov method, the pairing correlations over many single-particle orbits, which are treated by superposing Slater determinants in the usual MCSM, can be contained in individual basis vectors to a certain extent in the QVSM, which makes calculations for heavy nuclei more tractable.

Fig. 9 Extrapolation for the example of ^{64}Ge . (Modified from Fig. 4 of Shimizu et al. 2010)



Before discussing actual applications of the MCSM, a basic feature of the nuclear shell structure is discussed in the next section, for a more transparent understanding.

Shell Evolution Due to Monopole Interaction

The single-particle energies (SPEs), $\epsilon_{0;j}^p$ and $\epsilon_{0;j}^n$ in Eq. (4), are given, in the IPM of Mayer and Jensen, by the HO potential, the spin-orbit splitting, and the minor correction by the so-called ℓ^2 term (see Fig. 2). The SPEs are then constants within a given nucleus and vary only gradually as Z or N changes. In actual shell-model calculations, the SPEs are adjusted, in some cases, so as to describe experimental data such as the ground-state energies and level energies of excited states. However, as long as stable nuclei are concerned, the basic trends, such as the magic gaps and the orderings of single-particle orbits, do not differ from those depicted by Fig. 2.

The shell model, as the physics of many-body correlations rather than the IPM, includes an NN interaction in Eq. (5) and solves the Schrödinger equation in Eq. (6) for the Hamiltonian in Eq. (3). The SPEs are then crucial in determining the basic properties of the eigenstates, but it is also possible that such an NN interaction may change the SPEs in an effective way. This aspect has been discussed from early times, but its greater importance and wider appearance have been recognized in exotic nuclei, with emerging differences from the patterns shown in Fig. 2. The SPEs substantially vary as Z or N changes: in some cases, new magic numbers absent in Fig. 2 show up, while some conventional magic numbers are weakened or even disappear. Such phenomena are collectively called the **shell evolution** and occur due to particular basic features of the NN interaction. This section is devoted to the shell evolution: how it occurs and what consequences arise. The following part of this section is largely based on Otsuka (2022), as they are self-contained to a good extent.

Monopole Matrix Element and Monopole Interaction

The interaction \hat{V} in Eq. (5) can be decomposed, in general, into the two components: monopole and multipole interactions (Poves and Zuker 1981), irrespectively of its origin, derivation, or parameters. The monopole interaction is expressed in terms of the monopole matrix element defined for single-particle orbits j and j' as,

$$V^{\text{mono}}(j, j') = \frac{\sum_{(m, m')} \langle j, m ; j', m' | \hat{V} | j, m ; j', m' \rangle}{\sum_{(m, m')} 1}, \quad (20)$$

where m and m' are magnetic substates of j and j' , respectively, and the summation over m, m' is taken for all ordered pairs allowed by the Pauli principle. The monopole matrix element represents, as displayed schematically in Fig. 10, an orientation average for two nucleons in the orbits j and j' . See Otsuka et al. (2020) for more detailed and pedagogical descriptions.

The monopole interaction between two neutrons is given as the averaged interaction in this manner. For example, the monopole interaction between the two orbits $j \neq j'$ takes the following form,

$$V_{nn}^{\text{mono}}(j, j') \sum_{\mu, \mu'} a_{\mu}^{\dagger} a_{\mu'}^{\dagger} a_{\mu'} a_{\mu}, \quad (21)$$

where μ (μ') is a magnetic substate of the orbit j (j'). The monopole interaction between two neutrons can be expressed as

$$\hat{V}_{nn}^{\text{mono}} = \sum_j V_{nn}^{\text{mono}}(j, j) \frac{1}{2} \hat{n}_j^n (\hat{n}_j^n - 1) + \sum_{j < j'} V_{nn}^{\text{mono}}(j, j') \hat{n}_j^n \hat{n}_{j'}^n, \quad (22)$$

and the monopole interaction between two protons is given likewise. Based on the same definition and a certain manipulation of isospin properties (see Otsuka et al. 2020), the monopole interaction between a proton and a neutron can be given as,

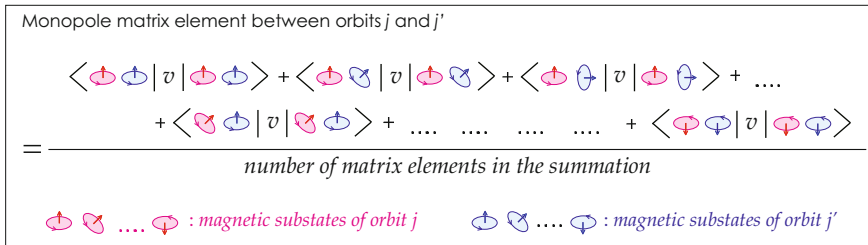


Fig. 10 Schematic illustration of the monopole matrix element. (Taken from Fig. 7 of Otsuka et al. 2020)

$$\begin{aligned} \hat{V}_{pn}^{\text{mono}} = & \sum_{j \neq j'} \frac{1}{2} \left\{ V_{T=0}^{\text{mono}}(j, j') + V_{T=1}^{\text{mono}}(j, j') \right\} \hat{n}_j^p \hat{n}_{j'}^n \\ & + \sum_j \frac{1}{2} \left\{ V_{T=0}^{\text{mono}}(j, j) \frac{2j+2}{2j+1} + V_{T=1}^{\text{mono}}(j, j) \frac{2j}{2j+1} \right\} \hat{n}_j^p \hat{n}_j^n, \end{aligned} \quad (23)$$

where $V_{T=0,1}^{\text{mono}}(j, j')$ stands, respectively, for the monopole matrix element for the isospin $T=0$ or 1 channel defined by Eq. (20) including isospin-symmetry effects (see Sec. III A of Otsuka et al. (2020) for details). Note that $V_{T=1}^{\text{mono}}(j, j')$ implies $V_{nn,pp}^{\text{mono}}(j, j')$. The second term on the RHS of Eq. (23) is slightly different from the first term on the RHS of Eq. (23) due to the special isospin property for the cases of $j=j'$. Obviously, $\hat{V}_{pn}^{\text{mono}}$ can be rewritten as

$$\hat{V}_{pn}^{\text{mono}} = \sum_{j,j'} \tilde{V}_{pn}^{\text{mono}}(j, j') \hat{n}_j^p \hat{n}_{j'}^n, \quad (24)$$

with $\tilde{V}_{pn}^{\text{mono}}(j, j')$ defined so as to reproduce Eq. (23).

The functional forms in Eqs. (22), (24) appear to be in accordance with the intuition from the averaging over all orientations: no dependences on angular properties (e.g. coupled J values) between the two interacting nucleons and the sole dependence on the number of particles in those orbits.

The monopole matrix elements can be expressed in an alternative but equivalent way as

$$V_T^{\text{mono}}(j, j') = \frac{\sum_J (2J+1) \langle j, j'; J, T | \hat{V} | j, j'; J, T \rangle}{\sum_J (2J+1)} \quad \text{for } T = 0 \text{ and } 1, \quad (25)$$

where $\langle j, j'; J, T | \hat{V} | j, j'; J, T \rangle$ implies TBMEs coupled to the angular momentum J and the isospin T (see Eq. (13)). It is noted that J takes here only even (odd) integers for $j = j'$ with $T = 1$ ($T = 0$). Supplemental Material Sec. S2 of Otsuka et al. (2020) presents a proof that this expression is indeed equivalent to the one discussed so far. The expression in Eq. (25) is more convenient in practical calculations, as the values of $\langle j, j'; J, T | \hat{V} | j, j'; J, T \rangle$ are explicitly handled usually.

The (total) monopole interaction is given by

$$\hat{V}^{\text{mono}} = \hat{V}_{pp}^{\text{mono}} + \hat{V}_{nn}^{\text{mono}} + \hat{V}_{pn}^{\text{mono}}, \quad (26)$$

and the monopole Hamiltonian is defined as

$$\hat{H}^{\text{mono}} = \hat{H}_0 + \hat{V}^{\text{mono}} = \sum_j \epsilon_{0,j}^p \hat{n}_j^p + \sum_j \epsilon_{0,j}^n \hat{n}_j^n + \hat{V}^{\text{mono}}. \quad (27)$$

The multipole interaction is introduced as

$$\hat{V}^{\text{multi}} = \hat{V} - \hat{V}^{\text{mono}}, \quad (28)$$

and the (total) Hamiltonian is written as

$$\hat{H} = \hat{H}^{\text{mono}} + \hat{V}^{\text{multi}}. \quad (29)$$

The multipole interaction becomes crucial in many aspects of nuclear structure, for instance, the shape deformation, as touched upon in later sections. The monopole interaction has been studied in many works, for example, Bansal and French (1964), Baranger (1970), Poves and Zuker (1981), Storm et al. (1983) (see Otsuka et al. 2020 for a brief description of the history).

The effective SPE (ESPE) of the proton (neutron) orbit j is introduced now. It is denoted by $\hat{\epsilon}_j^p$ ($\hat{\epsilon}_j^n$) and defined to be the change of the monopole Hamiltonian, \hat{H}^{mono} in Eq. (27), due to the addition of one proton (neutron) into the orbit j . It is still an operator. This change is nothing but the difference, when $n_j^{p,n}$ is replaced by $n_j^{p,n}+1$. For instance, the first term on the right-hand side (RHS) of Eq. (27) contributes to $\hat{\epsilon}_j^p$ by a constant, $\epsilon_{0;j}^p$. As another example, the RHS of Eq. (24) contributes by $\sum_{j'} \tilde{V}_{pn}^{\text{mono}}(j, j') \{(\hat{n}_j^p + 1) \hat{n}_{j'}^n - \hat{n}_j^p \hat{n}_{j'}^n\} = \sum_{j'} \tilde{V}_{pn}^{\text{mono}}(j, j') \hat{n}_{j'}^n$. Combining all terms, the ESPE of the proton orbit j is given as

$$\hat{\epsilon}_j^p = \epsilon_{0;j}^p + \sum_{j'} V_{pp}^{\text{mono}}(j, j') \hat{n}_{j'}^p + \sum_{j'} \tilde{V}_{pn}^{\text{mono}}(j, j') \hat{n}_{j'}^n. \quad (30)$$

The second and third terms on the RHS are contributions from valence protons and neutrons, respectively. The neutron ESPE is expressed likewise as

$$\hat{\epsilon}_j^n = \epsilon_{0;j}^n + \sum_{j'} V_{nn}^{\text{mono}}(j, j') \hat{n}_{j'}^n + \sum_{j'} \tilde{V}_{pn}^{\text{mono}}(j', j) \hat{n}_{j'}^p. \quad (31)$$

It is noted that in many actual cases, an appropriate expectation value of the ESPE operator is also called the ESPE with an implicit reference to some state characterizing the structure, e.g., the ground state.

The ESPE as an expectation value is often discussed in terms of the difference between two states, e.g., Ψ and Ψ' . The states Ψ and Ψ' may belong to the same nucleus or to two different nuclei. The formulas for this difference are discussed now. First the symbol $\Delta\mathcal{O}$ is introduced for an operator $\hat{\mathcal{O}}$ indicating the difference, $\langle \Psi | \hat{\mathcal{O}} | \Psi \rangle - \langle \Psi' | \hat{\mathcal{O}} | \Psi' \rangle$. Such differences of the ESPE values are expressed as

$$\Delta\epsilon_j^p = \sum_{j'} V_{pp}^{\text{mono}}(j, j') \Delta n_{j'}^p + \sum_{j'} \tilde{V}_{pn}^{\text{mono}}(j, j') \Delta n_{j'}^n, \quad (32)$$

and

$$\Delta\epsilon_j^n = \sum_{j'} V_{nn}^{\text{mono}}(j, j') \Delta n_{j'}^n + \sum_{j'} \tilde{V}_{pn}^{\text{mono}}(j', j) \Delta n_{j'}^p. \quad (33)$$

If Ψ' is a doubly closed shell and Ψ is an eigenstate with some valence protons and neutrons on top of this closed shell, these quantities stand for the evolution of ESPEs as functions of Z and N . Various physics cases can be studied with appropriate Ψ and Ψ' . Such ESPEs can provide picturesque prospects and great helps in intuitive understanding without resorting to complicated numerical calculations. This is an important aspect: the ESPE is not used in actual shell-model calculations but provides with intuitive physical pictures and overall sketches. The notion of the ESPE has been well utilized, for instance, in empirical studies in Grawe (2004), Sorlin and Porquet (2008), in certain ways related to the present article.

The interaction \hat{V} generally comprises several parts according to some classifications. The discussions in this subsection can be applied to each part separately: the monopole interaction of a particular part of \hat{V} can be extracted, and its resulting ESPEs can be evaluated. Examples are presented in the subsequent subsections.

It is noted that the definition of the ESPE can have certain variants with similar consequences, for instance, the combination of $n_j^{p,n} - 1/2$ and $n_j^{p,n} + 1/2$ instead of $n_j^{p,n}$ and $n_j^{p,n} + 1$.

Central, 2-Body Spin-Orbit and Tensor Parts of the NN Interaction

With the formulation presented above, a variety of subjects can be discussed, ranging from the shell structure, to the collective bands, and to the driplines. Let us start with the shell structure. While the discussions for Fig. 2 are based on basic nuclear properties, some aspects are missing. One of them is the orbital dependences of the monopole matrix element. This dependence generally appears but shows up more crucially in certain cases.

As shown below, some parts of the NN interaction, \hat{V} , show characteristic and substantial orbital dependences. Such parts can be specified in terms of their spin properties, as the NN interaction involves spin operator, an axial vector $\vec{\sigma}$ of nucleon. In the first part, no spin operator is included or spin operators are coupled to scalar terms, like $(\vec{\sigma}_1 \cdot \vec{\sigma}_2)$ with $\vec{\sigma}_{1,2}$ denoting the spin operator of the nucleon 1 or 2, and (\cdot) being a scalar product. This part is called the *central force*, and its effects are discussed in the next subsection. In the second part, spin operators are coupled to axial vectors. Such axial vectors must be coupled with other axial vectors such as the orbital angular momentum. The *2-body spin-orbit force* belongs to this category. Its effects are briefly commented in a later subsection, as the effects remain quite modest from the viewpoint of the shell evolution, except for special orbital combinations.

As presented in the second subsection from here, significant contributions arise from the *tensor force*, where spin operators are coupled to a (rank 2) tensor, $[\vec{\sigma}_1 \times \vec{\sigma}_2]^{(2)}$, where the last superscript means rank 2. This is a very complicated coupling, and this term must be coupled, in the interaction, with another (rank 2) tensor of the coordinates, in order to form a scalar. Similar terms appear in the electromagnetic interaction, but their effects are minor. The tensor force is, however, crucial in the nuclear case, partly because the dominant effect of the one-pion exchange process is a tensor force. Monopole properties of the tensor force are discussed below. It is noted that multiple-pion exchange processes are important origins of the central force part of the NN interactions.

Monopole Interaction of the Central Force

Now the monopole interaction of the central force component of NN interactions is discussed. Because the NN interaction is characterized by intermediate-range (~ 1 fm) attraction after modifications or renormalizations, the monopole matrix elements gain large magnitudes with negative sign (i.e., attractive), if radial wave functions of the single-particle orbits, j and j' in Eq. (20), are similar to each other. This similarity is visible, if these orbits are spin-orbit partners ($j = j_>$ and $j' = j_<$) with the identical radial wave functions (see Eq. (1)), for instance, $1f_{7/2}$ and $1f_{5/2}$. Another example is the coupling between unique-parity orbits, such as $1g_{9/2}$ and $1h_{11/2}$, for which the radial wave functions are similar because of no radial node. These types of strong correlations were pointed out by Federman and Pittel (1977), where the total effect of the 3S_1 channel of the NN interaction was discussed without the reference to the monopole interaction.

Monopole Interaction of the Tensor Force

Another important source of the monopole interaction with strong orbital dependences is the tensor force. The tensor force produces very unique effects on the ESPE. This is displayed in Fig. 11: the intuitive argument in Otsuka et al. (2005, 2020) proves that the monopole interaction of the tensor force is attractive between a nucleon in an orbit $j_<$ and another nucleon in an orbit $j'_>$, whereas it becomes repulsive for combinations, $(j_>, j'_>)$ or $(j_<, j'_<)$. The magnitude of such monopole interaction varies also. For example, it is strong in magnitude between spin-orbit partners, or between unique-parity orbits, etc. (Otsuka et al. 2020).

The ESPE is shifted in very specific ways as exemplified in Fig. 12b: if neutrons occupy a $j'_>$ orbit, the ESPE of the proton orbit $j_>$ is raised, whereas that of the proton orbit $j_<$ is lowered. This is nothing but a reduction of a proton spin-orbit splitting due to a specific neutron configuration. The amount of the shift is proportional to the number of neutrons in this configuration, as shown in Eq. (32) and in Fig. 12c. Other cases follow the same rule shown in Fig. 11. These general

Fig. 11 Monopole interaction of the tensor force. (Taken from Fig. 2 of Otsuka et al. 2005)

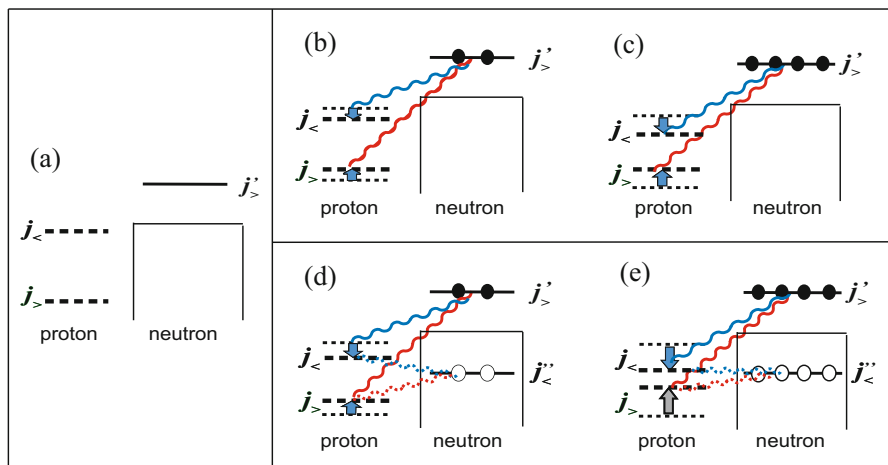
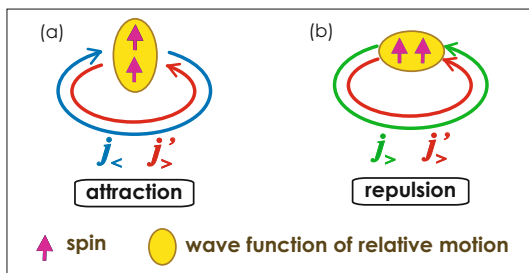


Fig. 12 Schematic picture of the ESPE change (i.e., shell evolution) due to the monopole interaction of the tensor force. (a) SPEs with no neutrons in the orbit $j'_{>}$. (b) The shifts of the proton ESPEs due to two (valence) neutrons in the orbit $j'_{>}$. (c) The same as (b) except for four neutrons. (d, e) Type II shell evolution due to neutron particle-hole excitations. (Taken from Fig. 1 of Otsuka and Tsunoda 2016)

features have been pointed out in Otsuka et al. (2005) with an analytic formula and an intuitive description of its origin.

Monopole Interaction Effects from the Central and Tensor Forces Combined

The combined effects of the central and tensor forces were discussed in Otsuka et al. (2010a) in terms of realistic shell-model interactions, USD (Brown and Wildenthal 1988) and GXPF1A (Honma et al. 2002, 2004). The V_{MU} interaction was then introduced as a general and simple shell-model NN interaction. Its central part consists of Gaussian interactions with spin/isospin dependences, and their strength parameters are determined so as to simulate the overall features of the monopole matrix elements of the central part of USD (Brown and Wildenthal 1988) and

GXPFI1A (Honma et al. 2002) interactions. Its tensor part is taken from the standard π - and ρ -meson exchange potentials (Bäckman et al. 1985; Osterfeld 1992; Otsuka et al. 2005). Thus, the V_{MU} interaction is defined as a function of the relative distance of two nucleons with spin/isospin dependences, which enables us to use it in a variety of regions of the nuclear chart, as shall be seen. A wide model space, typically a full HO shell or more, is required in order to obtain reasonable results, though.

Figure 13 depicts some examples: panel (a) displays the transition from a standard (*à la* Mayer-Jensen) $N=20$ magic gap to an exotic $N=16$ magic gap by plotting $\langle \hat{\epsilon}_j^n \rangle$ within the filling scheme (see Eq. (31)), as Z decreases from 20 to 8. The tensor monopole interaction between the proton $d_{5/2}$ and the neutron $d_{3/2}$ orbits plays an important role. The small $N=20$ magic gap for $Z=8-12$ is consistent with the island of inversion picture (see reviews, e.g., Caurier et al. 2005; Otsuka et al. 2020). Panel (b) depicts the inversion between the proton $f_{5/2}$ and $p_{3/2}$ orbits as N increases in Ni isotopes, by showing $\langle \hat{\epsilon}_j^p \rangle$ (see Eq. (30)). The figure exhibits exotically ordered single-particle orbits for $N > 44$. The tensor monopole interactions between the proton $f_{7/2,5/2}$ and the neutron $g_{7/2}$ orbits produce crucial effects. Panel (c) shows significant changes of the neutron single-particle levels from ^{90}Zr to ^{100}Sn , in terms of $\langle \hat{\epsilon}_j^n \rangle$. Without the tensor force, the near degeneracy of $g_{7/2}$ and $d_{5/2}$ orbits in ^{100}Sn does not show up.

These changes of the shell structure as a function of Z and/or N were collectively called *shell evolution* in Otsuka et al. (2005). The splitting between proton $g_{7/2}$ and $h_{11/2}$ in Sb isotopes shows a substantial widening as N increases from 64 to 82 as pointed out by Schiffer et al. (2004), which was one of the first experimental supports to the shell evolution partly because this was not explained otherwise. Note that while the origin of the shell evolution can be any part of the NN interaction, its appearance is exemplified graphically in Fig. 12a, b, c for the tensor force. The shell-evolution trend depicted in Fig. 13 appears to be consistent with experiment (ENSDF; Ichikawa et al. 2019; Liddick et al. 2006; Otsuka et al. 2010a, 2020; Sahin et al. 2017; Seweryniak et al. 2007). The monopole properties discussed

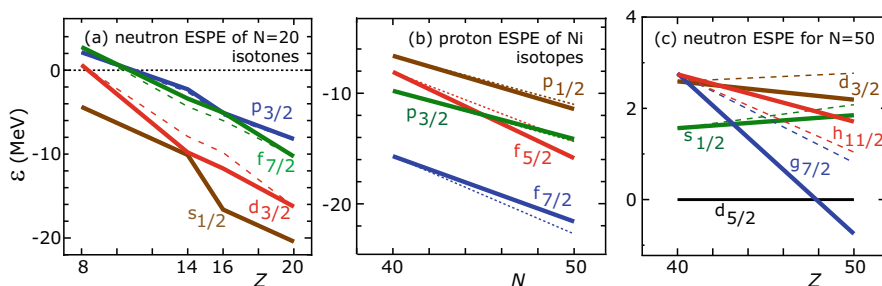


Fig. 13 Effective single-particle energies calculated by the V_{MU} interaction. The dashed lines are obtained by the central force only, while the solid lines include both the central force and the tensor force contributions. (Taken Fig. 3 of from Otsuka et al. 2010a)

in this subsection are consistent with the results shown by Smirnova et al. (2010) obtained through the spin-tensor decomposition (see, e.g., Otsuka et al. (2020) for some account).

Some of the emerging concepts were conceived in the study of exotic nuclei, particularly by looking at the shell structure and magic numbers of them. The obtained concepts were found later not to be limited to exotic nuclei but to be general. In this way, after the initial trigger by exotic nuclei, the overall picture of the shell structure has been renewed, and this section is devoted to a sketch of it with two major keywords, the *monopole interaction* and the *shell evolution*.

$N=34$ New Magic Number as a Consequence of the Shell Evolution

Among various cases of shell evolution, a notable impact was made by predicting a new magic number $N=34$. Figure 14 displays the shell evolution of some neutron single-particle orbits from Ni back to Ca isotopes, as Z decreases from 28 to 20. The $1f_{5/2}$ orbit is between the $2p_{3/2}$ orbit and the $2p_{1/2}$ orbit in Mayer-Jensen's shell model (see Fig. 2). By losing eight protons in Ni isotopes, this canonical shell structure is destroyed as the $1f_{5/2}$ orbit moves up above the $2p_{1/2}$ orbit. This movement of $1f_{5/2}$ orbit creates the $N=32$ gap as a by-product (Huck et al. 1985). The energy shift of the $1f_{5/2}$ orbit is due to the central and tensor forces by almost equal amounts. It is mentioned that the emergence of the $N=34$ magic number in Ca isotopes and the appearance of the Mayer-Jensen scheme in Ni isotopes are consistent from the viewpoint of the basic features of the NN interaction. The appearance of the $N=34$ magic number was predicted as a result of a spin-isospin interaction in Otsuka et al. (2001b). However, 12 years were required (Janssens 2005) until the experimental verification became feasible (Steppenbeck et al. 2013)

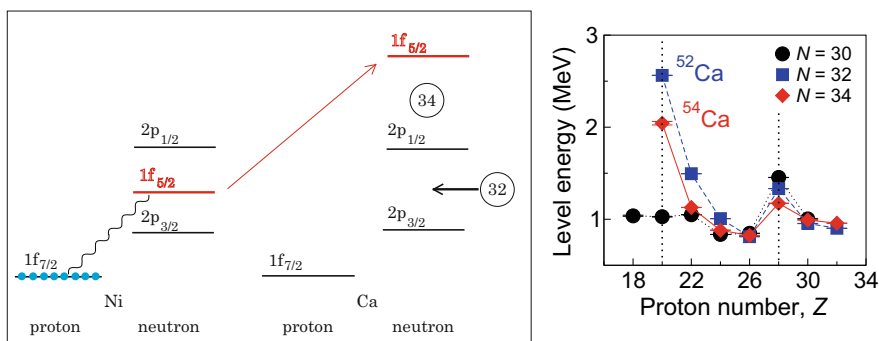


Fig. 14 (left) Schematic illustration of the shell evolution from Ni back to Ca for neutron orbits. Blue circles denote protons. The wavy line is the interaction between the proton $1f_{7/2}$ orbit and the neutron $1f_{5/2}$ orbit. The numbers in circles indicate magic numbers. (Taken from Fig. 3 of Otsuka and Tsunoda 2016). (right) Observed excitation energies of the 2_1^+ states. (Taken from Fig. 2 c of Steppenbeck et al. 2013)

(see Fig. 14 (right)). The measured 2^+ energy levels are included in Fig. 3b. More details are presented in Otsuka et al. (2020). Further evidences have been obtained recently by different experimental probes as reported in Michimasa et al. (2018) and Chen et al. (2019).

Monopole Interaction of the 2-Body Spin-Orbit Force

It is a natural question what effect can be expected from the 2-body spin-orbit force of the NN interaction. This force can be well described by the M3Y interaction, and its monopole effects were analyzed in detail in Otsuka et al. (2020), including its supplementary document. Although the monopole effects of this force contribute to the spin-orbit splitting (Otsuka et al. 2020), apart from this bulk-type property, its effect on the shell evolution is much weaker than the tensor force in most cases.

An interesting case is, however, found in the coupling between an s orbit and the $p_{3/2,1/2}$ orbits. There is no monopole effect from the tensor force, if an s orbit is involved. Instead, the s - p coupling due to 2-body spin-orbit force can be exceptionally strong as stressed in Otsuka et al. (2020) from both quantitative and intuitive viewpoints.

Monopole Interaction from the Three-Nucleon Force

The three-nucleon force (3NF) is currently of intense interest (see, for instance, a review Hammer et al. 2013). Among various aspects, Otsuka et al. (2010b) showed that one of the characteristic features of the monopole interaction of the effective NN interaction originates in the Fujita-Miyazawa 3NF (Fujita and Miyazawa 1957). A brief description is presented here (see Otsuka (2022) for a somewhat more detailed explanation). Figure 15a displays the effect of the Δ excitation in NN interaction. The Δ -hole excitation from the inert core changes the SPE of the orbit j as shown in panel (b) where m is one of the magnetic substates of the orbit j and m' means any state. This diagram renormalizes the SPE, and observed SPE should include this contribution. If there is a valence nucleon in the state m' as in panel (c), the process in panel (b) is Pauli-forbidden. However, in the shell-model and other nuclear structure calculations, the SPE containing the effect of panel (b) is used. One has to somehow incorporate the Pauli effect of panel (c), and a solution is the introduction of the process in panel (d). In this process, the state m' doubly appears in the intermediate state, but one can evaluate the Pauli effect by including panels (b) and (d) consistently. So, the process of panel (d) is included as an additional term to the effective NN interaction \hat{V} in Eqs. (3), (5). This is a usual mathematical trick and enables us to correctly treat the Pauli principle within the simple framework.

The actual modification of the effective NN interaction can be carried out in terms of the Fujita-Miyazawa 3NF. Panel (e) displays the Fujita-Miyazawa 3NF, but the states m and m' are assigned so that the situation in panel (d) is represented.

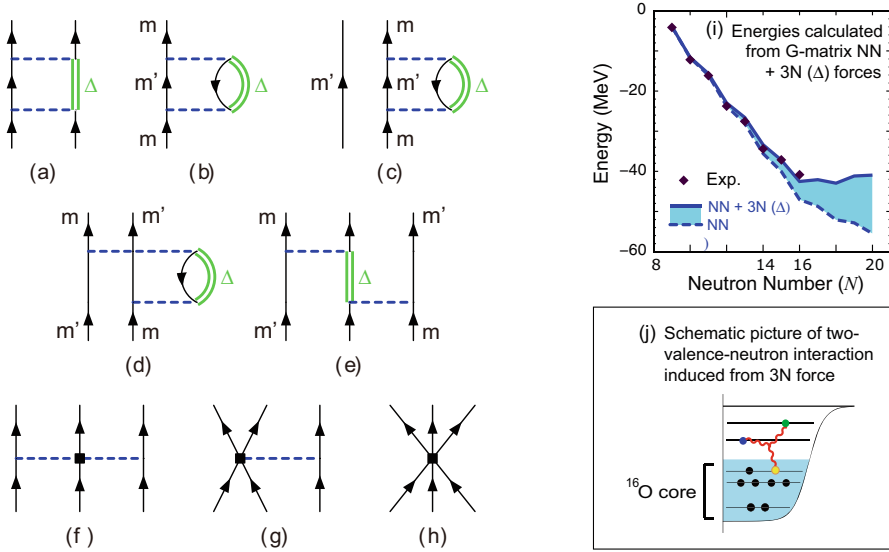


Fig. 15 Schematic illustration of the 3NF. (Based on Figs. 3 and 4 of Otsuka et al. 2010b)

Clearly the state m' appears in double, as mentioned above. If the nucleon line in the middle is taken for all the states in the inert core, panel (e) becomes equivalent to panel (d). By taking any possible magnetic substates for the left and right nucleon lines of panel (d), and summing over all inert-core states for the middle nucleon line, the modification to the effective NN interaction for valence nucleons can be introduced. The Pauli-blocking effect discussed above can then be incorporated by the monopole term of the present additional NN interaction. Naturally, the shell evolution due to the Δ -hole blocking is described by this particular monopole interaction obtained from the Fujita-Miyazawa 3NF. This monopole interaction is repulsive because of its origin in the blocking effect. (As a detail, it is noted that direct terms do not contribute to this monopole term because of parity-changing vertex for the pion exchange process (see Otsuka et al. 2005, 2010b).) The 3NF may also arise from other sources, but the main contribution to the shell evolution is expected to be generated by the present mechanism.

A similar treatment can be carried out in the chiral EFT framework. Panel (f) corresponds to panel (e), but the violation of Pauli principle is kind of hidden, because of a vertex in the middle (depicted by a square) instead of the Δ excitation.

In this argument, the 3NF produces a repulsive monopole NN interaction in the valence space, after the summation over the hole states of the inert core (see panel (j)), which corresponds to the normal ordering in other works. Panel (i) indicates an example of the repulsive effect on the ground-state energy of oxygen isotopes, locating the oxygen dripline at the right place or solving the oxygen anomaly (Otsuka et al. 2010b). This is rather strong repulsive monopole interaction, which is a consequence of inert core. This means that the present case is irrelevant to the

no-core shell model or other many-body approaches without the inert core (e.g., GFMC) (Carlson et al. 2015). This feature has caused some confusions in the past, but the difference is clear. The present repulsive monopole effect is much stronger than the other effects of the 3NF (Tsunoda et al. 2020), and the latter will be better clarified by further developments of the chiral EFT for 3NF in the future. It is noted that the present valence-space repulsive effect was noticed by Talmi in the 1960s (Talmi 1962).

Short Summary of This Section

The shell evolution is found in many isotopic and isotonic chains and sometimes results in the formation of new magic gaps or the disappearance of old ones, as departures from the IPM. Figure 3b displays the emergence of such new magic numbers $N=16$, 32, and 34. More changes may appear in the future studies. Interestingly, these findings are neither isolated nor limited to particular single-particle aspects but are related to other features of the nuclear structure as depicted below.

Correlations Among Valence Nucleons and Monte Carlo Shell Model

The NN interaction acting on valence nucleons produces the shell evolution through its monopole component. Besides this, it produces other important phenomena as combined effects of the monopole and multipole components (see Eq. (29)). These effects are linked to the mixings of different configurations of valence nucleons like the mixing between two configurations in Fig. 4 a-1 and a-2. Such configuration mixings are found in amplitudes in the vector in Eq. (11) and are caused by correlations among valence nucleons. Here the correlations mean that different configurations are superposed so as to gain certain many-body features. Of course, these correlations are consequences of the NN interaction. The energy gain by these correlations are often called *correlation energy*, for which the shell model seems to be advantageous over other models, because its solution is built directly on the NN interaction. This section sheds lights on some features of such correlations.

Shape Deformation, Quadrupole Interaction, and Rotational Band

The most visible outcome of the correlations is probably the surface deformation from a sphere, in particular ellipsoidal shapes or quadrupole deformations. The quadrupole deformation has been a very important subject since the 1950s, as initiated by Rainwater (1950) and by Bohr and Mottelson (Bohr 1952, 1975; Bohr and Mottelson 1953, 1969, 1975). In the shell model, the quadrupole deformation is considered to be driven by the quadrupole interaction, a part of the multipole

interaction in Eq. (28). However, the quadrupole interaction is a somewhat vague idea. It can mean the rank 2 component for the proton-neutron interaction, but this is already not applicable for the neutron-neutron or the proton-proton interactions because of ambiguities in the angular momentum recoupling. (The rank 2 component of the proton-neutron interaction means a part of this interaction comprising products of the proton and neutron one-body operators, each of which carries angular momentum 2. The coefficient of individual product is given by the NN interaction.)

Apart from such complexities in the interactions, there are certain features that can be simulated by the (scalar) coupling of the quadrupole-moment operators. In fact, the effects of the rank 2 part of the proton-neutron interaction may be approximated by those of such “quadrupole-moment interaction” particularly for low-lying states with strong quadrupole deformations, because fine details can be smeared out in coherent contributions from various configurations. Although the quadrupole-moment interaction with appropriately chosen strength parameters may be thus useful for intuitive interpretations or even simple calculations, the quadrupole interaction refers, in this article, to the rank 2 component of the proton-neutron interaction. The basic idea here is that the monopole (rank 0) and quadrupole (rank 2) interactions are taken from the common underlying NN interaction. The actual calculations for physical quantities are performed by including all other multipole interactions contained in realistic NN interactions, while the contributions of such other multipole interactions may be modest or negligible for low-lying ellipsoidally deformed states.

It is noted that the quadrupole-moment interaction was used in the SU(3) model for the sd shell (Elliott 1958a,b), the Pairing+QQ model (Bes and Sorensen 1969; Kumar and Baranger 1968), etc. It is also pointed out that rotational bands of atomic nuclei can be described with realistic NN interactions, as shown, for instance, Caurier et al. (1994), or even with ab initio interaction (Otsuka et al. 2022b).

If the quadrupole moments are larger, i.e., a stronger quadrupole deformation occurs, the nucleus gains more binding energy from the above argument on the quadrupole interaction. This is a very general phenomenon, and because of this mechanism, the ground and low-lying states of many nuclei are ellipsoidally deformed. Once the nucleus is deformed to an ellipsoid, this ellipsoid rotates and produces rotational bands, in the way analogous to the Nambu-Goldstone mechanism.

Type II Shell Evolution

Among many aspects of the surface deformation, the discussions here are focused on the crossroad of the deformation and the shell evolution. The shell evolutions shown in Fig. 12b and c occur, respectively, due to the addition of two or four neutrons into the orbit $j'_>$. Instead of adding, one can put neutrons into the orbit $j'_>$ by taking the neutrons out of some orbits below $j'_>$ or equivalently by creating

holes there, as shown in Fig. 12d. If such a lower orbit happens to be the $j'_{<}$ orbit as in Fig. 12d, its monopole matrix elements show just the opposite trends compared the $j'_{>}$ orbit. However, because holes are created in $j'_{<}$, the sign of the monopole-interaction effect is reversed, and the final effect has the same sign as the monopole effect from the orbit $j'_{>}$ (see Fig. 12d). Thus, the particle-hole (ph) excitation of the two neutrons in Fig. 12d reduces the proton $j_{>-}j_{<-}$ splitting even more than in Fig. 12b. This reduction becomes stronger with the ph excitations of four neutrons, as depicted in Fig. 12e. Such strong reduction of the spin-orbit splitting produces interesting consequences beyond shell structure changes. This type of the shell structure change within the same nucleus is called **Type II shell evolution**.

A Doubly Closed Nucleus ^{68}Ni

The type II shell evolution was first discussed for ^{68}Ni in Tsunoda et al. (2014b). Figure 16 shows the theoretical and experimental energy levels of ^{68}Ni . The theoretical results were obtained with the A3DA-m interaction through the Monte Carlo shell model (MCSM) calculation. It is noted that the theoretical calculations presented in the following parts of this section are obtained by the A3DA-m interaction unless otherwise mentioned.

Because $Z=28$ is an SO magic number and $N=40$ is an HO magic number (see Fig. 2), the ground state of ^{68}Ni is primarily a doubly closed shell. Indeed, in the theoretical ground state, the neutron pf -shell is completely occupied with a large probability (54%), although the neutron $g_{9/2}$ orbit holds about one neutron in average ($\sim 2 \times 0.46$) as a consequence of the correlations due to the NN interaction. In contrast, the 0_3^+ state located at the excitation energy, $\text{Ex} \sim 3 \text{ MeV}$, is the band head of a rotational band of an ellipsoidal shape. The neutron pf -shell closure is severely broken, with the occupation number of the neutron $g_{9/2}$ orbit being as large

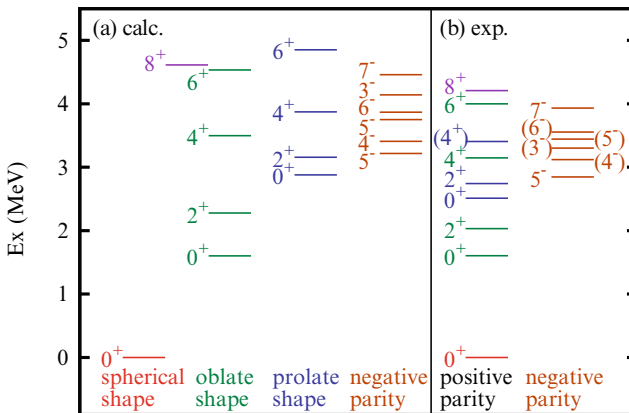


Fig. 16 Level scheme of ^{68}Ni . (Taken from Fig. 2 of Tsunoda et al. 2014b)

as ~ 4 . The mechanism shown in Fig. 12e is emerging in this case, reducing the proton $f_{5/2}$ - $f_{7/2}$ splitting. A reduced splitting facilitates the configuration mixing between these two orbits, which can produce notable effects on the quadrupole deformation as stated below.

Deformed Shapes and Potential Energy Surface

The energy of ^{68}Ni is illustrated in Fig. 17 (left) for various ellipsoidal shapes, *spherical*, *prolate*, *oblate*, and in between (called *triaxial*), which will be explained below. The energy is calculated by the constrained Hartree-Fock (CHF) calculation with the same shell-model Hamiltonian as in Fig. 16. The imposed constraints are given in terms of the quadrupole moments in the intrinsic (body-fixed) frame, denoted by Q_0 and Q_2 (Bohr and Mottelson 1975), to be discussed now.

The ellipsoid “observed” in the intrinsic frame can be schematically illustrated as in Fig. 18 with the (x, y, z) axes of the intrinsic (body-fixed) frame. There is a freedom to choose these axes. In this article, the traditional convention is adopted: the (x, y, z) axes are assigned so that the three principal axes of the ellipsoid are placed on the (x, y, z) axes, with the relation $R_z \geq R_x \geq R_y$ where (R_x, R_y, R_z) denote, respectively, the lengths of the three principal axes (Bohr and Mottelson 1975). Figure 18b depicts the general situation of this assignment. If $R_z \geq R_x = R_y$ holds, the shape is called prolate. A special case of $R_z = R_x > R_y$ is displayed in Fig. 18c, which corresponds to an oblate shape. If two of the principal axes have the same lengths, the shape is called axially symmetric. The shapes other than the prolate and oblate shapes are called triaxial, except for the trivial spherical shape.

For a classical uniform density ellipsoid, the quadrupole moments are expressed as

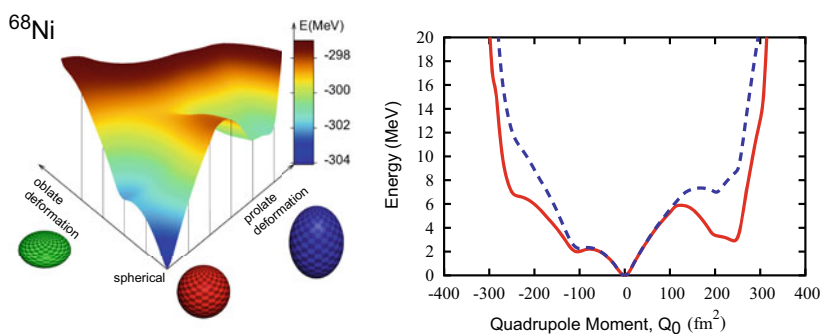


Fig. 17 (left) Potential energy surface (PES) of ^{68}Ni . (Taken from Fig. 5 of Otsuka and Tsunoda 2016). (right) PES of ^{68}Ni for axially symmetric shapes. The solid line shows the PES of the full Hamiltonian, whereas the dashed line is the PES with practically no tensor force contribution. (Taken from Fig. 6 of Otsuka and Tsunoda 2016)

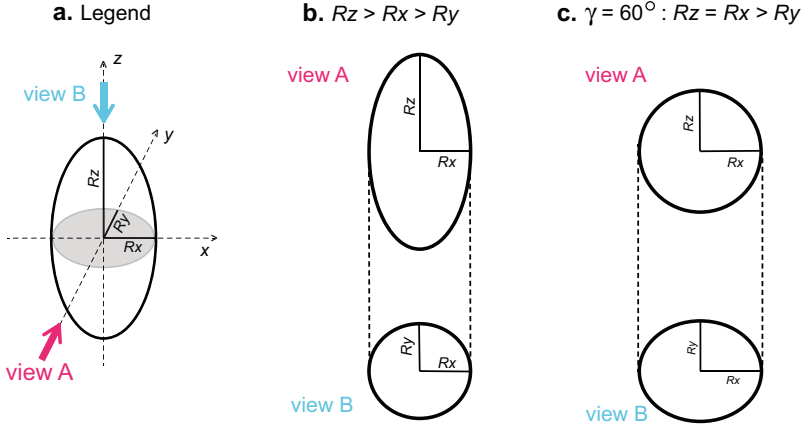


Fig. 18 Schematic illustration of ellipsoids of uniform-density matter. The principal axes, R_x , R_y , and R_z of the x , y , and z axes are indicated, respectively. (a) Legend indicating that the views A and B are along the y and z axes, respectively. (b) The general case with $R_z > R_x > R_y$ is displayed. (c) A special case with $R_z = R_x > R_y$ is shown

$$Q_0 = \int_V dx dy dz (2z^2 - x^2 - y^2) \rho_0, \quad (34)$$

and

$$Q_2 = \sqrt{3/2} \int_V dx dy dz (x^2 - y^2) \rho_0, \quad (35)$$

where ρ_0 is the value of the uniform density and V to the integral symbol means the interior of the ellipsoid. With the above convention, both Q_0 and Q_2 are positive definite (or zero).

Moving back to the quantum mechanics, for a given state η in the intrinsic frame, a matrix is calculated as

$$\begin{pmatrix} \langle \eta | \sum_i (x^2)_i | \eta \rangle & \langle \eta | \sum_i (xy)_i | \eta \rangle & \langle \eta | \sum_i (xz)_i | \eta \rangle \\ \langle \eta | \sum_i (yx)_i | \eta \rangle & \langle \eta | \sum_i (y^2)_i | \eta \rangle & \langle \eta | \sum_i (yz)_i | \eta \rangle \\ \langle \eta | \sum_i (zx)_i | \eta \rangle & \langle \eta | \sum_i (zy)_i | \eta \rangle & \langle \eta | \sum_i (z^2)_i | \eta \rangle \end{pmatrix}, \quad (36)$$

where the index, i , runs over all valence nucleons. The (x, y, z) axes are redefined so that this hermitian matrix becomes diagonal. The principal axes are placed on the new (x, y, z) axes, so as to fulfill the relation among the eigenvalues: $R_z \geq R_x \geq R_y$ with $R_z = \sqrt{(5/3) \langle \sum_i (z^2)_i \rangle}$, etc. The two intrinsic quadrupole moments are then given, similarly to Eqs. (34) and (35), by

$$Q_0 = \langle \eta | \sum_i (2z^2 - x^2 - y^2)_i | \eta \rangle, \quad (37)$$

and

$$Q_2 = \sqrt{3/2} \langle \eta | \sum_i (x^2 - y^2)_i | \eta \rangle, \quad (38)$$

where the index, i , runs over all valence nucleons. (See, e.g., Ring and Schuck (1980) for more technical details about the intrinsic shapes.) Note that the nucleons in the closed shell do not contribute to the quadrupole moments.

Because of the construction of the intrinsic frame, Q_0 and Q_2 are positive definite or zero. If the state η is invariant with respect to the rotation about the z axis of the intrinsic frame, the relation $Q_2=0$ holds. As $Q_0 \geq 0$, this quantum mechanical case is also called the prolate shape, consistently with the classical prolate case of $R_x = R_y$ in Fig. 18b. Such axially symmetric prolate shapes have been believed to be dominant in heavy nuclei, but a different picture is emerging in recent years, as sketched later.

Figure 18c depicts the axially symmetric oblate shapes: the wave function is invariant with respect to the rotation about the y axis. This case can be described, equivalently, by exchanging the R_z and R_y axes (see, for instance, Ring and Schuck (1980) for details). This exchange makes Q_0 negative (because of $R_z < R_y, R_x$) and $Q_2 = 0$. In fact, by this exchange, Q_0 is replaced by $-\sqrt{Q_0^2 + 2Q_2^2}$. This expression of the oblate shape is sometimes used, as seen just below. It is noted that the physics does not change between the two ways of describing the ellipsoidal properties.

The plot of the CHF energy against Q_0 and Q_2 is called the potential energy surface (PES). Figure 17 (left) exhibits an example. The distance from the origin stands for $\sqrt{Q_0^2 + 2Q_2^2}$. The Q_0 value increases from 0 along the axis toward the blue symbol, where $Q_2 = 0$ is kept, representing prolate shapes.

The Q_2 value is indicated by the angle from the axis of $Q_0 > 0$ and $Q_2 = 0$, and the value of this angle is given by

$$\gamma = \arctan \{ \sqrt{2} Q_2 / Q_0 \}. \quad (39)$$

The γ value is positive or zero in the default convention, where $Q_{0,2} \geq 0$. The range $0^\circ \leq \gamma \leq 60^\circ$ is sufficient (Ring and Schuck 1980). The axis toward the green object in Fig. 17 (left) corresponds to $\gamma = 60^\circ$, which is nothing but the axially symmetric oblate case and can be expressed by negative Q_0 and $Q_2=0$ as discussed just above.

The minimum energy in Fig. 17 (left) is found at the spherical shape (red sphere), where $Q_0=Q_2=0$. The constraints are changed to a more prolate deformed ellipsoid (blue object in Fig. 17(left) along the upper-right axis (“prolate deformation” in the figure), where Q_0 increases but $Q_2=0$ is kept. This means that the vertical axis

(z axis) of the blue object is the stretched direction of the ellipsoid, and the cross section of the ellipsoid perpendicular to this axis is a circle. The green object in Fig. 17(left) is shrunk in the y axis, and the cross section perpendicular to it is a circle, an oblate axially symmetric deformation. The green object is placed so that its y axis is vertical. The area in between represents a wide area of triaxial deformations. In most of the discussions of this section, the axially symmetric deformation is assumed for the sake of simplicity, but the triaxiality is discussed later for other nuclei.

Figure 17(left) shows that as Q_0 is increased from $Q_0=0$ to the upper right direction, the energy relative to the minimum energy climbs up by 6 MeV. This is because protons and neutrons must be excited across the magic gaps from the doubly closed shell in order to create states producing imposed Q_0 values. After reaching the local peak or the “pass,” the energy starts to come down. It is lowered by 3 MeV from this “pass” to a “basin,” or the area around the local minimum. This lowering is due to the quadrupole interaction. Beyond the basin, the effect of the quadrupole interaction is saturated, and it cannot compete the energy needed for exciting more protons and neutrons across the gaps to fulfill the constraints. This explanation is the usual one for the appearance of the deformed local minimum in the PES. The appearance of two (or more) different shapes with rather small energy difference is one of the phenomena frequently seen in atomic nuclei and is called the shape coexistence (see a review Heyde and Wood (2011), for instance). The shape coexistence is seen, in the energy levels and the PES, between the spherical ground state and the prolate deformed excited state now. The quadrupole interaction is undoubtedly among the essential factors of the shape coexistence. But this may not be a full story.

Figure 17 (right) exhibits the same energy along the axes of the left panel. In the right half of the right panel, Q_0 is varied from 0 fm^2 to 400 fm^2 while $Q_2=0$ is kept. The left half of the right panel stands for $\gamma = 60^\circ$, oblate shapes. As discussed above, another convention with the y and z exchanged is taken so that the ellipsoidal deformation is described with negative Q_0 values and $Q_2 = 0$. Thus, Fig. 17 (right) shows Q_0 from -400 fm^2 to 400 fm^2 , which actually represents the two axes in Fig. 17 (left) connecting the green to the red and to the blue objects. The red solid line shows the CHF results of the full Hamiltonian, whereas for the dashed line, the tensor monopole interactions between the neutron ($g_{9/2}$, $f_{5/2}$) orbits and the proton ($f_{5/2}$, $f_{7/2}$) orbits are practically removed. This removal means no effects depicted in Fig. 12d, e. The dashed line displays a less pronounced prolate local minimum at weaker deformation with much higher excitation energy. The significant difference between the solid and dashed lines suggests that the monopole effects are crucial to lower this local minimum and stabilize it. Some details of the mechanism for this difference are touched upon now. With the tensor monopole interaction, once sufficient neutrons are in $g_{9/2}$, the proton $f_{5/2}$ - $f_{7/2}$ splitting is reduced. As the quadrupole interaction generally tends to mix different single-particle orbits, this reduced splitting facilitates the effects driven by the quadrupole interaction, leading to stronger quadrupole deformations. Thus, type II shell evolution increases the

deformation. The tensor monopole interaction involving the neutron $g_{9/2}$ orbit produces extra binding energy, if more protons are in $f_{5/2}$ and less are in $f_{7/2}$. This extra binding energy lowers the deformed states, otherwise they are high in energy because of the energy cost for promoting neutrons from the pf shell to $g_{9/2}$ due to single-particle energies. Thus, a strong interplay emerges between the monopole interaction and the quadrupole interaction, and type II shell evolution strengthens this interplay. It enhances the deformation and lowers the energy of deformed states. Without this interplay, as indicated by blue dashed line in Fig. 17 (right), the local minimum is pushed up by 2 MeV and may be dissolved into the sea of many other states not shown in the PES. It is obvious that this interplay mechanism works self-consistently.

Deformation Parameters and Comparison to Calculations with Gogny Interaction

The deformation parameters, β_2 and γ , are introduced now, as more direct measures of the quadrupole deformation carried by wave functions.

The axis lengths, R_z , R_y , and R_x , are parametrized (Bohr and Mottelson 1975) by variables, R_0 , β_2 , and γ ,

$$R_z = \{1 + 0.63 \beta_2 \cos \gamma\} R_0, \quad (40)$$

$$R_x = \{1 + 0.63 \beta_2 \sin(\gamma - 30^\circ)\} R_0, \quad (41)$$

$$R_y = \{1 - 0.63 \beta_2 \cos(60^\circ - \gamma)\} R_0, \quad (42)$$

where R_0 is the average of $R_{x,y,z}$ and β_2 , called *deformation parameter*, represents the magnitude of the ellipsoidal deformation from the sphere ($\beta_2=0$). The angle γ is the same as the one introduced in Eq. (39), as explained below. It is known that the range $\gamma = 0^\circ - 60^\circ$ suffices to specify the ratios among R_x , R_y , and R_z .

The parameter β_2 represents the magnitude of the ellipsoidal deformation from a sphere. The β_2 is sometimes denoted by β for brevity. The value of β_2 can be obtained, in some approximation, from Q_0 and Q_2 obtained in the shell model calculation. Such Q_0 and Q_2 values are appropriate for analyzing the properties of the shell-model states formulated in the given model space. The β_2 value, however, represents the actual shape of the nucleus and is connected to its actual quadrupole moments. As the shell-model quadrupole moments are transformed to the actual values by in-medium (e.g., core-polarization) corrections, the β_2 value is obtained, in a reasonable approximation, through the formula (Utsuno et al. 2015),

$$\beta_2 = \sqrt{5/16\pi} \{(e + e'_p + e'_n)/e\} (4\pi/3 R_0^2 A^{5/3}) \sqrt{(Q_0)^2 + 2(Q_2)^2}, \quad (43)$$

where e is the unit charge, e'_p (e'_n) denotes proton (neutron) effective charge induced by in-medium effects, and R_0 stands for the radius parameter of the droplet model (see Otsuka et al. (2022a) for some detailed explanation). Here, Q_0 and Q_2 imply the quadrupole moments of the valence-nucleon system, and in-medium correction is needed as represented by the multiplication factor $(e + e'_p + e'_n)/e$, where the e'_p and e'_n appear in symmetric way, because the matter quadrupole moments are relevant rather than the charge ones. The value of the parameter γ does not change from the one in Eq. (39), because Q_0 and Q_2 are rescaled by the same amount. The relations in Eqs. (43) and (39) have been shown to work very well in many studies, for instance, Leoni et al. (2017), Mărginean et al. (2020), Marsh et al. (2018), Otsuka et al. (2019), Tsunoda and Otsuka (2021).

Figure 19b shows the PES for $^{68-78}\text{Ni}$ as a function of β_2 (β in the figure) assuming the axial symmetry, in comparison to the corresponding PES obtained by the calculation with the Gogny interaction (Girod et al. 1988). The convention of $Q_0 < 0$ (i.e., $\beta_2 < 0$) and $Q_2 = 0$ (i.e., $\gamma = 0$) is taken for axially symmetric oblate shapes, with β_2 ranging from ~ -0.5 to ~ 0.5 . The energy minimum for ^{68}Ni is adjusted to be equal between the two calculations, as indicated by blue thin solid line. Both the present and the Gogny calculations produce similar PES curves near the minima. The local bump appears around $\beta_2 = 0.2-0.3$ in the prolate side in both calculations. The major difference arises for the local minimum around $\beta_2 \sim 0.4$: its excitation energy appears to be higher than 5 MeV for the Gogny calculation (pink dashed line in Fig. 19), whereas it is lower than 3 MeV in the present calculation (red solid line in Fig. 19). This notable difference is ascribed, to a large extent, to the type II shell evolution driven by the tensor interaction. The tensor interaction is included in the present calculation, whereas not (at least explicitly) in the Gogny calculation. This observation is consistent with the major conclusion obtained from Fig. 17 (right). The difference between the two calculations becomes smaller as moving from ^{68}Ni to ^{78}Ni . This trend is natural because the neutron excitations from the pf -shell are suppressed as the $1g_{9/2}$ orbits are filled by more neutrons, and consequently the type II shell evolution occurs more weakly. It is noted that the oblate local minima gain the energy through the monopole tensor force, but the effect is smaller.

T-Plot Analysis

The PES discussed so far is very useful but cannot pin down shapes carried by individual MCSM wave functions. This subsection is devoted to a powerful methodology for this purpose, called *T-plot* (Tsunoda et al. 2014b).

Each basis vector $\Phi_i(J^\pi)$ in Eq. (14) has intrinsic quadrupole moments,

$$\langle \Phi_i(J^\pi) | \hat{Q}_0 | \Phi_i(J^\pi) \rangle \quad \text{and} \quad \langle \Phi_i(J^\pi) | \hat{Q}_2 | \Phi_i(J^\pi) \rangle, \quad (44)$$

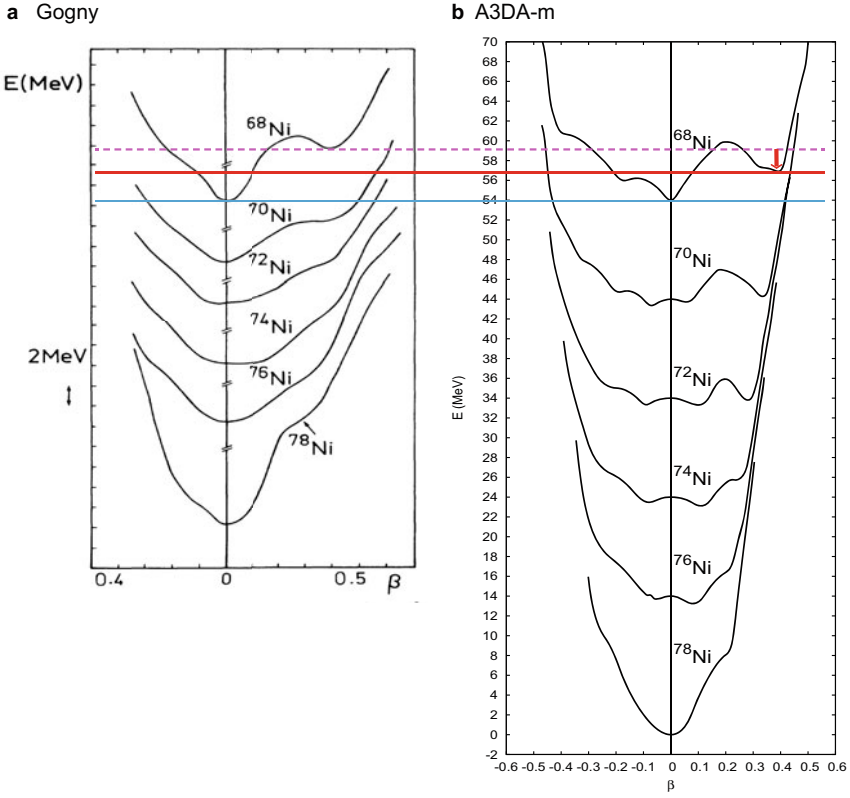


Fig. 19 Potential energy surface (PES) of $^{68-78}\text{Ni}$ with axially symmetric shapes. **(a)** PES by the Gogny interaction. (Taken from Fig. 4 of Girod et al. 1988). **(b)** PES by the A3DA-m interaction. The horizontal thin blue, thick red, and pink dashed lines indicate, respectively, the lowest energy, the prolate local minimum in panel (b), and the same one in panel (a), for ^{68}Ni

where $\hat{Q}_{0,2}$ imply the operators for $Q_{0,2}$ mentioned above. It is assumed that the axes of the intrinsic frame are taken according to the default convention, i.e., the traditional way. The T-plot circle for $\Phi_i(J^\pi)$ is placed according to those values on the PES. The area of the circle is proportional to the overlap probability with the eigenstate of interest, Ψ , as shown in Eq. (14). Such T-plot circles are displayed in Fig. 20 for $^{68-78}\text{Ni}$. The small yellow circles are located at the (Q_0, Q_2) values of MCSM basis vectors, with their sizes representing their relevance to the eigenstate, as stated above. With the relations in Eqs. (43) and (39), the T-plot can utilize the (β_2, γ) as partial but useful labeling of the basis vector in Eq. (14). The fully correlated eigenstates are described in terms of (β_2, γ) with their mean values and fluctuations with respect to quadrupole shapes. The evolution of nuclear shapes is clearly seen in Fig. 20. Certain advantages of mean-field approaches are now nicely incorporated into the shell model.

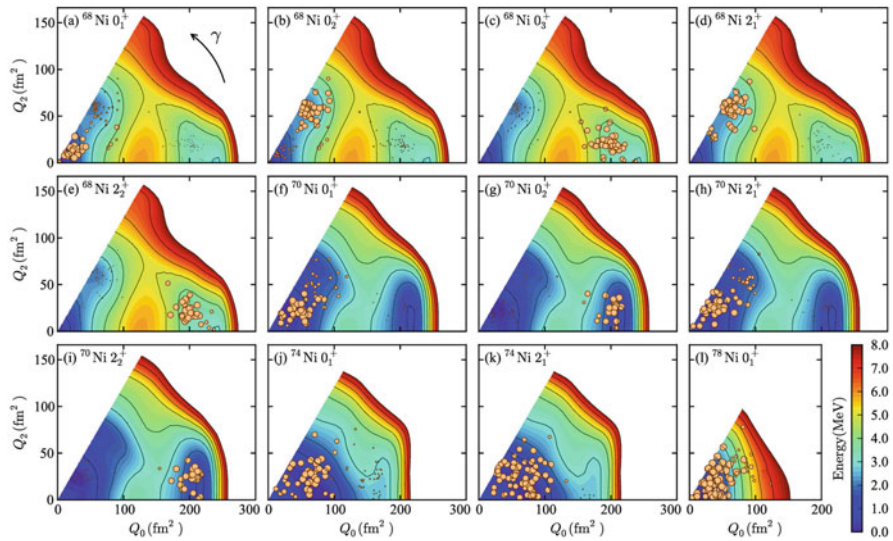


Fig. 20 PES and T-plot for $^{68-78}\text{Ni}$. (Taken from Fig. 3 of Tsunoda et al. 2014b)

Figure 20 shows that the T-plot circles are concentrated near the spherical limit for the ground state of ^{68}Ni . The ^{68}Ni nucleus has three 0^+ states of different characters: spherical, oblate, and prolate. The 2_1^+ and 2_2^+ states depict, respectively, T-plot patterns similar to those of the 0_2^+ and 0_3^+ states, as a clear indication of the formation of collective bands. The prolate local minimum disappears in ^{74}Ni and beyond. The ^{78}Ni nucleus shows a steep minimum, but the T-plot pattern of the ground state shows notable fluctuations. The fluctuations in ^{78}Ni are stronger than those in ^{68}Ni , and this difference is understood by the jj (LS) neutron closed shell for ^{78}Ni (^{68}Ni) where the dynamical quadrupole deformation occurs (does not occur) over the magic gap at $N=50$ (40). This subtlety of magic SO and HO magic numbers is a fascinating feature.

Lighter Ni isotopes have been studied with the same Hamiltonian as the one for Fig. 20. The obtained T-plot circles are shown, in a three-dimensional plot, in Fig. 21 for ^{66}Ni (Leoni et al. 2017). The same set of the MCSM basis vectors is used for the four 0^+ states. The white circles represent the MCSM basis vectors mainly forming the ground state, while the red circles indicate those mainly composing the 0_4^+ state, which is strongly deformed. Although there is no local minimum for oblate shapes, the T-plot circles of the major MCSM basis vectors for the 0_2^+ state are concentrated around moderately oblate shapes (green circles).

It is mentioned that the intrinsic shapes are also analyzed, in the method of Poves et al. (2020), within the conventional shell model by using Kumar invariants of quadrupole matrix elements for a set of the eigenstates belonging to the (almost) same shape.

Fig. 21 PES and T-plot for ^{66}Ni . (Taken from Fig. 1 of Leoni et al. (2017))

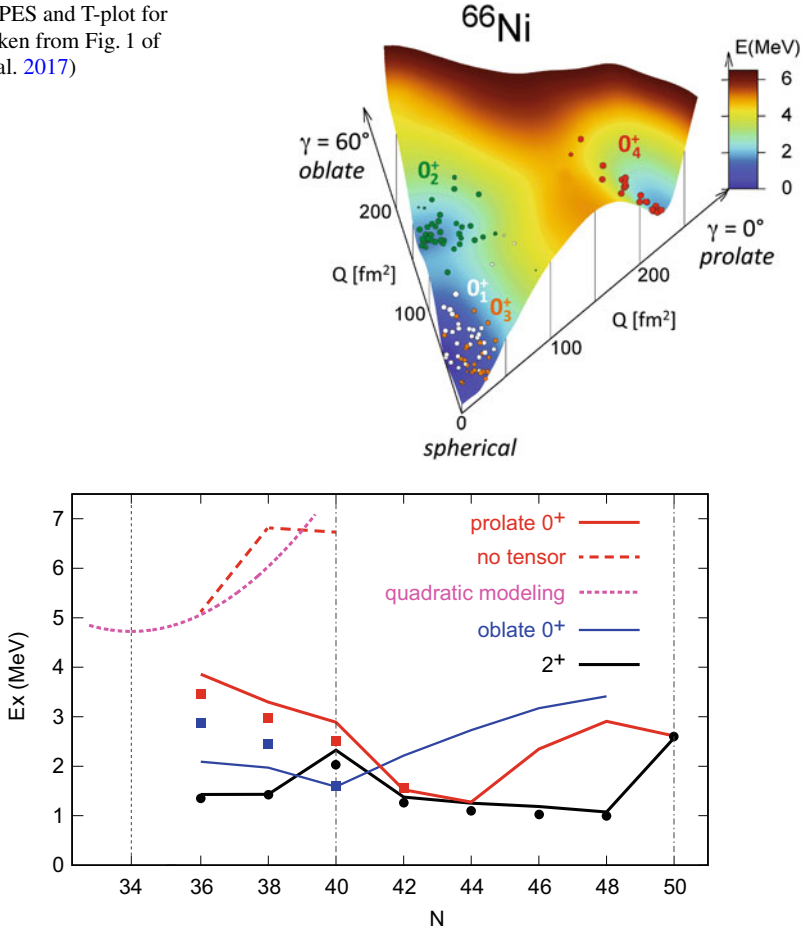


Fig. 22 Excitation energies for $^{64-78}\text{Ni}$. Symbols are experimental data. Lines are theoretical calculations. The excitation energies of strongly prolate deformed states are shown by red squares and line. Those of moderately oblate deformed states are shown by blue squares and line. Black circles and line indicate the excitation energies of the 2_1^+ states. The estimated excitation energies of strongly prolate deformed states calculated without major monopole contributions of the tensor force are shown by red dashed line. Pink dotted line indicates the simple modeling of deformed intruder states (see the text), with parameters fitted to the estimated values without the tensor force effect

It is of interest how the prolate deformed state changes its excitation energy as the neutron number, N , is varied within the Ni isotopes. Figure 22 displays the calculated excitation energies of the 2_1^+ , oblate 0^+ , and prolate 0^+ states, in comparison to experimental counterparts, for example, those obtained by Flavigny et al. (2015), Leoni et al. (2017), Mărginean et al. (2020), Morales et al. (2017), where the shape assignment may be subject to further confirmation. The 2_1^+ levels

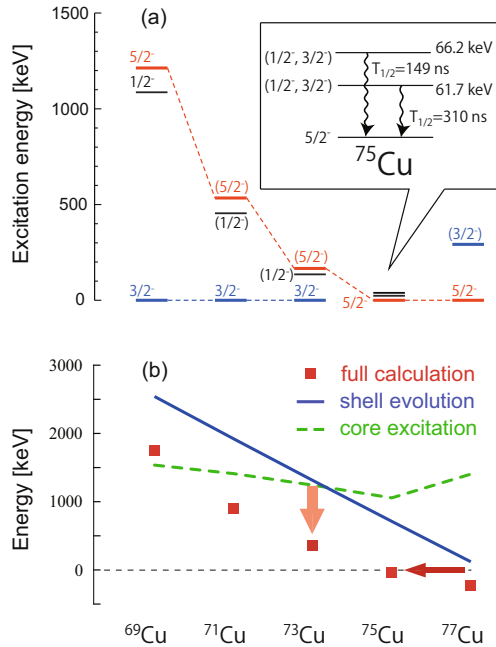
go down fast as N departs from $N=40$ in both sides (except for $N=50$) and then stay nearly constant, as reproduced well by the present calculation. It is noted that the levels of ^{78}Ni are calculated by another Hamiltonian (see Taniuchi et al. 2019). The prolate deformed 0^+ state shows a pattern of particular interest. As this state gains binding energies from the deformation, it is expected to come down as N moves away from the $N=40$ magic number, because the deformation tends to become stronger toward the middle of the shell, which is considered to be at $N=34$, a half way down to $N=28$. In fact, this 0^+ state comes down in energy as N increases from 40. On the contrary, the prolate 0^+ state is shifted higher in energy as N decreases from 40, and moreover this trend is described well by the present MCSM calculation. In order to understand the meanings of this trend unexpected in a sense, the excitation energy is estimated with the Hamiltonian without major tensor force effects (Otsuka and Tsunoda 2016). Figure 17 depicts that the excitation energy of the prolate state of ^{68}Ni is raised by ~ 4 MeV if the tensor force effect is cut off. Similarly, the excitation energies without major tensor force effects are estimated for $^{64,66}\text{Ni}$ as shown by red dashed line in Fig. 22. The trend can be compared to what is expected conventionally. In fact, the conventionally expected trend is modeled by a parabola like $Ex \sim a(N - N_c)^2 + b$ where a and b are parameters, N denotes the neutron number, and N_c implies N for the middle of the relevant shell. In the present case, the major shell $N = 28 - 40$ is taken, yielding $N_c=34$. The pink dotted line represents how such a simple model looks like, where the present result for $N=36$ and the average of them for $N=38$ and 40 are used to fix the parameters a and b . As this is an extremely simple modeling, its predictions cannot be very quantitative. Nevertheless, it is of interest that for $N=34$, its prediction is close to the extrapolation of the red line, the actual MCSM results.

It is natural that type II shell evolution is weakened as N becomes smaller from $N=40$, because the neutron Fermi surface becomes far below the $g_{9/2}$ orbit reducing neutron excitations from the pf -shell to the $g_{9/2}$ orbit. In this way, the “unexpected” trend of the prolate-state excitation energy for $N < 40$ can be naturally understood. Thus, the present systematic trend further supports the crossroad scenario between the monopole and quadrupole (deformation) effects. It is of interest to clarify the trends further away in both sides of Fig. 22 as well as in other regions of the nuclear chart.

Shell Evolution and Surface Deformation

The shell evolution discussed earlier in this article can, in principle, be washed away by correlations produced by the shell-model NN interaction. The inversion between the $3/2_1^-$ and $5/2_1^-$ states in Cu isotopes is discussed from the viewpoint of the straightforward shell evolution in Fig. 13b. This inversion can be studied in the presence of such correlations. Figure 23 shows the energy of the $5/2_1^-$ state relative to the $3/2_1^-$ state as a result of the full diagonalization of the A3DA-m Hamiltonian, as a function of the neutron number. The spacing between the $3/2_1^-$ and $5/2_1^-$ states is reduced from the shell-evolution estimate due to the monopole interaction

Fig. 23 Shell evolution in neutron-rich Cu isotopes. **(a)** Experimental systematics of energy levels for odd-*A* Cu isotopes. Inset exhibits experimental details. **(b)** Calculated energy levels of the $5/2_1^-$ state relative to the $3/2_1^-$ state, in three different methods with the same Hamiltonian, A3DA-m. The red squares depict the MCSM calculation with full of correlations, whereas the blue line indicates the shell evolution assuming the simple filling configuration in the $g_{9/2}$ orbit of neutrons. The green dashed line represents the MCSM calculation without major shell evolution effects. (Taken from Fig. 1 of Ichikawa et al. 2019)



(see “shell evolution” in Fig. 13b). This reduction is basically a consequence of the correlations due to the multipole interaction in the shell-model calculation, which are primarily, in this case, the excitations of the corresponding Ni core. The magnitude of these correlation effects does not change much as a function of the neutron number. In fact, if the monopole interaction relevant to this inversion is removed from the NN interaction, the shell model calculation produces the excitation energy of the $5/2_1^-$ state equal to 1–1.5 MeV (see “core excitation” in Fig. 13b), leading to no inversion. Thus, it is clear that the shell evolution mechanism lowers the $5/2_1^-$ state as the neutron number increases, while the core excitation yields a kind of background shift, being constant to a good extent, of the excitation energy.

More details of the core excitation can be visualized by T-plots as shown in Fig. 24. The T-plot is quite similar between a given Cu isotope and its Ni core. This similarity suggests that the odd proton does not disturb the Ni core too much, which is consistent with the almost constant shift of the $3/2_1^-$ - $5/2_1^-$ energy difference, shown in Fig. 23. The validity of the MCSM wave functions is verified by the magnetic moments (see Fig. 25), where the experimental values agree with the MCSM value.

The prolate strongly deformed states of ^{68,70}Ni isotopes discussed above are formed on top of massive particle-hole excitations. Figure 24 suggests that no T-plot circles appear for large (Q_0 , Q_2) values in the $3/2_1^-$ or $5/2_1^-$ state. Modest particle-hole excitations are seen experimentally in ⁷⁷Cu (Sahin et al. 2017) and

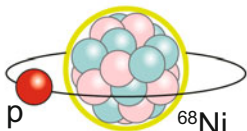
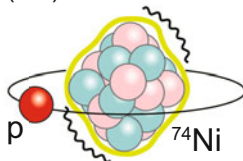
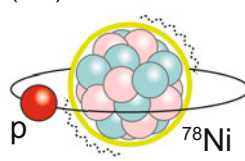
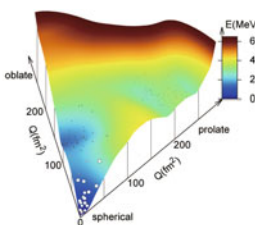
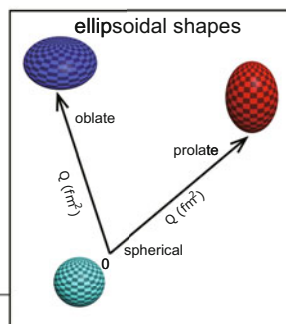
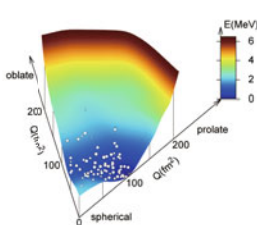
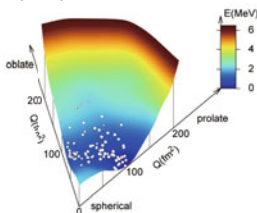
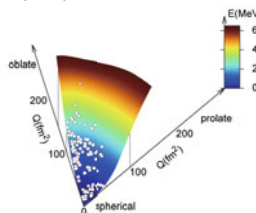
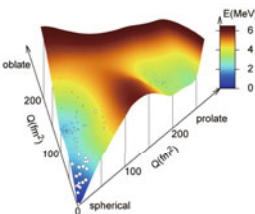
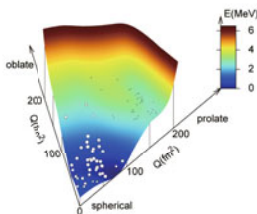
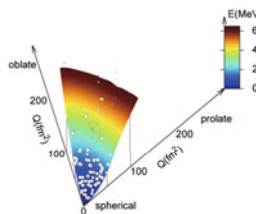
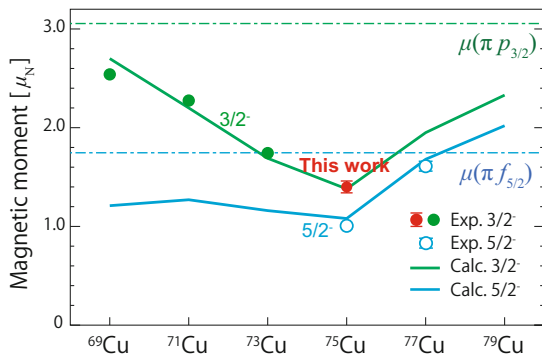
a. Schematic view : proton and core(a-1) ^{69}Cu (a-2) ^{75}Cu (a-3) ^{79}Cu **b. $3/2^-$ states in Cu isotopes**(b-1) ^{69}Cu (b-2) ^{75}Cu **c. $5/2^-$ states in Cu isotopes**(c-1) ^{75}Cu (c-2) ^{79}Cu **d. Ground states (0^+) in Ni isotopes**(d-1) ^{68}Ni (d-2) ^{74}Ni (d-3) ^{78}Ni 

Fig. 24 T-plots of Ni and Cu isotopes. (a) Schematic illustrations of the Ni core and the odd proton. (b, c) For $^{69,75,79}\text{Cu}$ isotopes, the $3/2^-$ and $5/2^-$ states are shown. (d) The corresponding Ni ground states are taken. (Taken from Fig. 4 of Ichikawa et al. 2019)

Fig. 25 Magnetic moments of Cu isotopes. “This work” in the figure means the measured value reported in Ichikawa et al. (2019). (Taken from Fig. 3 of Ichikawa et al. 2019)



⁷⁹Cu (Olivier et al. 2018) isotopes with rather clear separation from the low-lying the $3/2^-$ and $5/2^-$ states, suggesting that the $Z=28$ gap still remains for such lowest states as shown in Fig. 13b.

Short Summary of This Section

Type II shell evolution occurs in various cases, especially in a number of shape coexistence cases, providing deformed intruder states with stronger deformation, lower excitation energies, and more stabilities. It is an appearance of the monopole-quadrupole interplay and plays crucial roles in various phenomena in other nuclei including the first-order phase transition (Zr isotopes Kremer et al. 2016; Singh et al. 2018; Togashi et al. 2016), the second-order phase transition (Sn isotopes Togashi et al. 2018), and the multiple even-odd phase transitions (Hg isotopes Marsh et al. 2018).

The shell model can describe the monopole-quadrupole interplay, including type II shell evolution, as far as the model space is sufficiently wide and the Hamiltonian is realistic. This advantage becomes more important in other subjects of nuclear structure, being one of the front lines of the shell model studies. In some of such cutting-edge calculations, the merging of conventional shells occurs as shown in Fig. 4b, which may open new scopes but may bring more difficulties to actual computations.

Remarks

The major purpose of this article is to present a quick overview of the contemporary shell model studies, starting from a scratch. Quite often, for the shell model, computed numbers and computational feasibility are regarded as the shell model itself, but this does not fully cover what the shell model can provide. Although the computational capability of the shell model is very important and even crucial to

some studies of nuclear physics, the shell model has provided and can provide us with clear, useful and sometimes novel pictures or ideas for a variety of facets of the nuclear structure. These merits have been developed partly by importing models and concepts of other theories of nuclear structure such as mean field models. In this sense, the contemporary shell model is a combined product of various models and theories of nuclear structure. Along this line, there are quite a few developments in recent years, including new pictures of collective rotational bands in heavy nuclei (Otsuka et al. 2019), new mechanism of neutron driplines (Tsunoda et al. 2020), and new view of the α -clustering in light nuclei (Otsuka et al. 2022b). These are reviewed in a compact form (Otsuka 2022) or reported very recently, and are not discussed in this article.

Acknowledgments This work was supported in part by MEXT as “Program for Promoting Researches on the Super computer Fugaku” (Simulation for basic science: from fundamental laws of particles to creation of nuclei) and by JICFuS. This work was supported by JSPS KAKENHI Grant Numbers JP19H0514, JP21H00117.

References

- M. Agostini, G. Benato, J.A. Detwiler, J. Menéndez, F. Vissani, *Toward the Discovery of Matter Creation with Neutrinoless Double-Beta Decay* (2022). arXiv:2202.01787v1 [hep-ex]
- K. Arnsward et al., Phys. Lett. B **772**, 599 (2017)
- A. Arima, S. Cohen, R.D. Lawson, M.H. Macfarlane, Nucl. Phys. A **108**, 94 (1968)
- S.-O. Bäckman, G.E. Brown, J.A. Niskanen, Phys. Rep. **124**, 1 (1985)
- R.K. Bansal, J.B. French, Phys. Lett. **11**, 145 (1964)
- M. Baranger, Nucl. Phys. A **149**, 225 (1970)
- G. Bertsch, J. Borysowicz, H. McManus, W.G. Love, Nucl. Phys. A **284**, 399 (1977)
- D.R. Bes, R.A. Sorensen, *Advances in Nuclear Physics*, vol. 2, ed. by M. Baranger, E. Vogt (Plenum, New York, 1969; Springer, Berlin, 2012), pp. 129–222
- S. Bogner, T.T.S. Kuo, L. Coraggio, A. Covello, N. Itaco, Phys. Rev. C **65**, 051301 (2002)
- S.K. Bogner, R.J. Furnstahl, A. Schwenk, Prog. Part. Nucl. Phys. **65**, 94 (2010)
- N. Bohr, Nature **137**, 344 (1936a)
- N. Bohr, Nature **137**, 351 (1936b)
- N. Bohr, Science **86**, 161 (1937)
- A. Bohr, Mat. Fys. Medd. Dan. Vid. Selsk. **26**, 14 (1952)
- A. Bohr, *Nobel Lectures, Physics 1971–1980*, ed. by S. Lundqvist (World Scientific, Singapore, 1992), pp. 213–232
- A. Bohr, B.R. Mottelson, Mat. Fys. Medd. Dan. Vid. Selsk. **27**, 16 (1953)
- A. Bohr, B.R. Mottelson, *Nuclear Structure I* (Benjamin, New York, 1969)
- A. Bohr, B.R. Mottelson, *Nuclear Structure II* (Benjamin, New York, 1975)
- B.A. Brown, Phys. Rev. Lett. **85**, 5300 (2000)
- B.A. Brown, W.D.M. Rae, Nucl. Data Sheets **120**, 115 (2014)
- B.A. Brown, W.A. Richter, Phys. Rev. C **74**, 034315 (2006)
- B.A. Brown, B.H. Wildenthal, Annu. Rev. Nucl. Part. Sci. **38**, 29 (1988)
- B.A. Brown, N.J. Stone, J.R. Stone, I.S. Towner, M. Hjorth-Jensen, Phys. Rev. C **71**, 044317 (2005)
- J. Carlson et al., Rev. Mod. Phys. **87**, 1067 (2015)
- E. Caurier, F. Nowacki, Acta Phys. Polon. B **30**, 705 (1999)
- E. Caurier, A. Zuker, A. Poves, G. Martínez-Pinedo, Phys. Rev. C **50**, 225 (1994)
- E. Caurier, G. Martínez-Pinedo, F. Nowacki, A. Poves, A.P. Zuker, Rev. Mod. Phys. **77**, 427 (2005)

- S. Chen et al., Phys. Rev. Lett. **123**, 142501 (2019)
- S. Cohen, D. Kurath, Nucl. Phys. **73**, 1 (1965)
- L. Coraggio, A. Covello, A. Gargano, N. Itaco, Phys. Rev. C **80**, 021305 (2009)
- J.P. Elliott, Proc. R. Soc. **245**, 128 (1958a)
- J.P. Elliott, Proc. R. Soc. **245**, 562 (1958b)
- Evaluated nuclear structure data file*, <http://www.nndc.bnl.gov/ensdf/>
- P. Federman, S. Pittel, Phys. Lett. B **69**, 385 (1977)
- F. Flavigny et al., Phys. Rev. C **91**, 034310 (2015)
- J. Fujita, H. Miyazawa, Prog. Theor. Phys. **17**, 360 (1957)
- A. Gade, T. Glasmacher, Prog. Part. Nucl. Phys. **60**, 161 (2008)
- M. Girod, P. Dessagne, M. Langevin, F. Pougheon, P. Roussel, Phys. Rev. C **37**, 2600 (1988)
- H. Grawe, in *The Euroschool Lectures on Physics with Exotic Beams*, vol. I, ed. by J. Al-Khalili, E. Roeckl (Springer, Berlin/Heidelberg, 2004), pp. 33–75
- H.-W. Hammer, A. Nogga, A. Schwenk, Rev. Mod. Phys. **85**, 197 (2013)
- O. Haxel, J.H.D. Jensen, H.E. Suess, Phys. Rev. **75**, 1766 (1949)
- H. Hergart, S.K. Bogner, T.D. Morris, A. Schwenk, K. Tsukiyama, Phys. Rep. **621**, 165 (2016)
- K. Heyde, *The Nuclear Shell Model* (Springer, Berlin, 1994)
- K. Heyde, *Basic Ideas and Concepts in Nuclear Physics: An Introductory Approach* (Institute of Physics Publishing, London, 2004)
- K. Heyde, J.L. Wood, Rev. Mod. Phys. **83**, 1467 (2011)
- M. Hjorth-Jensen, T.T.S. Kuo, E. Osnes, Phys. Rep. **261**, 125 (1995)
- M. Honma, T. Mizusaki, T. Otsuka, Phys. Rev. Lett. **75**, 1284 (1995)
- M. Honma, T. Otsuka, B.A. Brown, T. Mizusaki, Phys. Rev. C **65**, 061301(R) (2002)
- M. Honma, T. Otsuka, B.A. Brown, T. Mizusaki, Phys. Rev. C **69**, 034335 (2004)
- M. Honma, T. Otsuka, T. Mizusaki, M. Hjorth-Jensen, Phys. Rev. C **80**, 064323 (2009)
- A. Huck, G. Klotz, A. Knipper, C. Miehé, C. Richard-Serre, G. Walter, A. Poves, H.L. Ravn, G. Marguier, Phys. Rev. C **31**, 2226 (1985)
- Y. Ichikawa et al., Nat. Phys. **15**, 321 (2019)
- R.V.F. Janssens, Nature **435**, 897 (2005)
- C.W. Johnson, W.E. Ormand, P.G. Krastev, Comput. Phys. Commun. **184**, 2761 (2013)
- C. Kremer et al., Phys. Rev. Lett. **117**, 172503 (2016)
- K. Kumar, M. Baranger, Nucl. Phys. A **110**, 529 (1968)
- T.T.S. Kuo, G.E. Brown, Nucl. Phys. **85**, 40 (1966)
- S.M. Lenzi, F. Nowacki, A. Poves, K. Sieja, Phys. Rev. C **82**, 054301 (2010)
- S. Leoni et al., Phys. Rev. Lett. **118**, 162502 (2017)
- S.N. Liddick et al., Phys. Rev. Lett. **97**, 082501 (2006)
- R. Machleidt, D.R. Entem, Phys. Rep. **503**, 1 (2011)
- B.A. Marsh et al., Nat. Phys. **14**, 1163 (2018)
- M.G. Mayer, Phys. Rev. **75**, 1969 (1949)
- S. Michimasa et al., Phys. Rev. Lett. **121**, 022506 (2018)
- A.I. Morales et al., Phys. Lett. B **765**, 328 (2017)
- S. Märginean et al., Phys. Rev. Lett. **125**, 102502 (2020)
- T. Nakamura, H. Sakurai, H. Watanabe, Prog. Part. Nucl. Phys. **97**, 53 (2017)
- A. Nogga, S.K. Bogner, A. Schwenk, Phys. Rev. C **70**, 061002 (2004)
- L. Olivier et al., Phys. Rev. Lett. **119**, 192501 (2018)
- F. Osterfeld, Rev. Mod. Phys. **64**, 491 (1992)
- T. Otsuka, Physics **4**, 258 (2022)
- T. Otsuka, Y. Tsunoda, J. Phys. G **43**, 024009 (2016)
- T. Otsuka, T. Mizusaki, M. Honma, Phys. Rev. Lett. **81**, 1588 (1998)
- T. Otsuka, M. Honma, T. Mizusaki, N. Shimizu, Y. Utsuno, Prog. Part. Nucl. Phys. **47**, 319–400 (2001)
- T. Otsuka, R. Fujimoto, Y. Utsuno, B.A. Brown, M. Honma, T. Mizusaki, Phys. Rev. Lett. **87**, 082502 (2001)
- T. Otsuka, T. Suzuki, R. Fujimoto, H. Grawe, Y. Akaishi, Phys. Rev. Lett. **95**, 232502 (2005)

- T. Otsuka, T. Suzuki, M. Honma, Y. Utsuno, N. Tsunoda, K. Tsukiyama, M. Hjorth-Jensen, Phys. Rev. Lett. **104**, 012501 (2010)
- T. Otsuka, T. Suzuki, J.D. Holt, A. Schwenk, Y. Akaishi, Phys. Rev. Lett. **105**, 032501 (2010)
- T. Otsuka, Y. Tsunoda, T. Abe, N. Shimizu, P. Van Duppen, Phys. Rev. Lett. **123**, 222502 (2019)
- T. Otsuka, A. Gade, O. Sorlin, T. Suzuki, Y. Utsuno, Rev. Mod. Phys. **92**, 015002 (2020)
- T. Otsuka, N. Shimizu, Y. Tsunoda, Phys. Rev. C **105**, 014319 (2022)
- T. Otsuka, T. Abe, T. Yoshida, Y. Tsunoda, N. Shimizu, N. Itagaki, Y. Utsuno, J. Vary, P. Maris, H. Ueno, Nat. Commun. **13**, 2234 (2022)
- A. Poves, A. Zuker, Phys. Rep. **70**, 235 (1981)
- A. Poves, F. Nowacki, Y. Alhassid, Phys. Rev. C **101**, 054307 (2020)
- I. Ragnarsson, S. Nilsson, *Shapes and Shells in Nuclear Structure* (Cambridge University Press, Cambridge, 1995)
- J. Rainwater, Phys. Rev. **79**, 432 (1950)
- W.A. Richter, S. Mkhize, B.A. Brown, Phys. Rev. C **78**, 064302 (2008)
- P. Ring, P. Schuck, *The Nuclear Many-Body Problem* (Springer, Berlin, 1980)
- E. Sahin et al., Phys. Rev. Lett. **118**, 242502 (2017)
- J.P. Schiffer et al., Phys. Rev. Lett. **92**, 162501 (2004)
- D. Seweryniak et al., Phys. Rev. Lett. **99**, 022504 (2007)
- N. Shimizu, Genshikaku Kenkyu (in Japanese) **58**, 96 (2013)
- N. Shimizu, Y. Utsuno, T. Mizusaki, T. Otsuka, T. Abe, M. Honma, Phys. Rev. C **82**, 061305(R) (2010)
- N. Shimizu, T. Abe, Y. Tsunoda, Y. Utsuno, T. Yoshida, T. Mizusaki, M. Honma, T. Otsuka, Prog. Theor. Exp. Phys. **2012**, 01A205 (2012)
- N. Shimizu, T. Abe, M. Honma, T. Otsuka, T. Togashi, Y. Tsunoda, Y. Utsuno, T. Yoshida, Phys. Scr. **92**, 063001 (2017)
- N. Shimizu, T. Mizusaki, T. Utsuno, Y. Tsunoda, Comput. Phys. Commun. **244**, 372 (2019)
- N. Shimizu, Y. Tsunoda, Y. Utsuno, T. Otsuka, Phys. Rev. C **103**, 014312 (2021)
- P. Singh et al., Phys. Rev. Lett. **121**, 192501 (2018)
- N.A. Smirnova, B. Bally, K. Heyde, F. Nowacki, K. Sieja, Phys. Lett. B **686**, 109 (2010)
- O. Sorlin, M.-G. Porquet, Prog. Part. Nucl. Phys. **61**, 602 (2008)
- D. Steppenbeck et al., Nature **502**, 207 (2013)
- M. Storm, A. Watt, R. Whitehead, J. Phys. G **9**, L165 (1983)
- K. Takayanagi, Nucl. Phys. A **852**, 61 (2011a)
- K. Takayanagi, Nucl. Phys. A **864**, 91 (2011b)
- I. Talmi, Rev. Mod. Phys. **34**, 704 (1962)
- R. Taniuchi et al., Nature **569**, 53 (2019)
- T. Togashi, Y. Tsunoda, T. Otsuka, N. Shimizu, Phys. Rev. Lett. **117**, 172502 (2016)
- T. Togashi, Y. Tsunoda, T. Otsuka, N. Shimizu, M. Honma, Phys. Rev. Lett. **121**, 062501 (2018)
- Y. Tsunoda, T. Otsuka, Phys. Rev. C **103**, L021303 (2021)
- N. Tsunoda, K. Takayanagi, M. Hjorth-Jensen, T. Otsuka, Phys. Rev. C **89**, 024313 (2014)
- Y. Tsunoda, T. Otsuka, N. Shimizu, M. Honma, Y. Utsuno, Phys. Rev. C **89**, 031301(R) (2014)
- N. Tsunoda, T. Otsuka, N. Shimizu, M. Hjorth-Jensen, K. Takayanagi, T. Suzuki, Phys. Rev. C **95**, 021304(R) (2017)
- N. Tsunoda, T. Otsuka, K. Takayanagi, N. Shimizu, T. Suzuki, Y. Utsuno, S. Yoshida, H. Ueno, Nature **587**, 66 (2020)
- Y. Utsuno, N. Shimizu, T. Otsuka, T. Yoshida, Y. Tsunoda, Phys. Rev. Lett. **114**, 032501 (2015)